Nonlinear Flow Affects Hydrodynamic Forces and Neutrophil Adhesion Rates in Cone–Plate Viscometers

Harish Shankaran and Sriram Neelamegham

Bioengineering Laboratory, Department of Chemical Engineering, State University of New York at Buffalo, Buffalo, New York 14260 USA

ABSTRACT   We present a theoretical and experimental analysis of the effects of nonlinear flow in a cone–plate viscometer. The analysis predicts that flow in the viscometer is a function of two parameters, the Reynolds number and the cone angle. Nonlinear flow occurs at high shear rates and causes spatial variations in wall shear stress, collision frequency, interparticle forces and attachment times within the viscometer. We examined the effect of these features on cellular adhesion kinetics. Based on recent data (Taylor, A. D., S. Neelamegham, J. D. Hellums, et al. 1996. *Biophys. J.* 71:3488–3500), we modeled neutrophil homotypic aggregation as a process that is integrin-limited at low shear and selectin-limited at high shear. Our calculations suggest that selectin and integrin on-rates lie in the order of 10^{-2}–10^{-4}/s. They also indicate that secondary flow causes positional variations in adhesion efficiency in the viscometer, and that the overall efficiency is dependent not only on the shear rate, but also the sample volume and the cone angle. Experiments performed with isolated neutrophils confirmed these predictions. In these experiments, enhancing secondary flow by increasing the sample volume from 100 to 1000 μl at 1500/s for a 2° cone caused up to an ~45% drop in adhesion efficiency. Our results suggest that secondary flow may significantly influence cellular aggregation, platelet activation, and endothelial cell mechanotransduction measurements made in the viscometer over the range of conditions applied in typical biological studies.

GLOSSARY

General note on notations: All vector and tensor quantities are in boldface, while their corresponding components are in plain text with the component index written as a subscript within brackets. For example **G** is a tensor and $G_{(11)}$ is its component. Variables in particle-fixed coordinates are written as primed variables (e.g. **G**′ is the velocity gradient tensor in particle-fixed coordinates).

C_p; $C(r_i^*, \beta_j)$; $\bar{C}$ = number of collisions experienced by a particle per unit time; collision frequency in number of collisions per unit time per unit volume at node point (i, j); volume-averaged collision frequency for the entire viscometer

dA = differential area element on the collision sphere

$F'_{(3)}$; f_c = interparticle normal force; bond-strength

$F_{max}(r_i^*, \beta_j)$; $\bar{F}_{max}$ = maximum normal force at the node (i, j) in the viscometer; collision-averaged maximum normal force for the entire viscometer

G; **G**; **G**′ = shear rate; velocity gradient tensor; velocity gradient tensor in particle-fixed coordinates

k_b; k_f^0; k_r^0 = Boltzmann's constant; forward rate of bond formation; intrinsic reverse rate

M, N = total number of grid points in the radial and vertical directions of the viscometer

n = unit outward normal vector to the surface of the collision sphere

N_b; N_b^{crit}; N_L = number of receptor–ligand bonds; critical number of bonds required to hold the doublet together; ligand density in intercellular contact area

N_{col}; N_P = total number of weighted-random collision orientations generated for the collision frequency calculations; particle concentration in the viscometer

Re = Reynolds number

R; r; r^*; r_i^* = cone radius; radial distance of a point in the viscometer; dimensionless radial distance = r/R; dimensionless radial position of the ith radial grid point in the viscometer

r$_c$ = position vector of an element on the collision sphere in space-fixed coordinates

R_T = number of receptors per cell

$\mathbf{S}; \mathbf{S}'$ = rate-of-strain tensor in space-fixed coordinates; rate-of-strain tensor in particle-fixed coordinates

$\mathbf{u}_C$ = relative velocity between the centers of colliding spheres in space-fixed coordinates

u, v, w = fluid velocity components in the radial (r), vertical (θ), and azimuthal (ϕ) directions, respectively

$V; V(r_i^*, \beta_j)$ = sample volume being sheared in the viscometer; volume associated with the (i, j)th node point in the viscometer

X_v, Y_v, Z_v = reference cartesian coordinate axes for the viscometer (Fig. 1)

Greek Symbols

$\alpha; \beta; \beta_j$ = cone angle; angle measurement in the θ direction in the viscometer (Fig. 1). By definition $\beta = \pi/2 - \theta$; angular position of the jth vertical grid point

γ = bond interaction parameter

$\eta(r_i^*, \beta_j); \bar{\eta}$ = adhesion efficiency at the node point (i, j) in the viscometer; overall collision-averaged adhesion efficiency for the entire viscometer

$\mu; v$ = viscosity; kinematic viscosity of fluid being sheared

$\theta; \phi$ = polar and azimuthal angles in the spherical coordinate system used in the solution for flow in the viscometer (Fig. 1)

$\theta_1, \phi_1; \theta_1^0, \phi_1^0$ = polar and azimuthal angles describing the orientation of a doublet (see Fig. 1a in Arp and Mason, 1977); initial particle collision orientation

$\Omega; \Omega_S$ = cone angular velocity; particle angular velocity vector in space-fixed coordinates

$\tau; \tau_r; \tau_\phi; \tau_{tot}$ = wall shear stress at the plate surface; its components in the radial direction; and the azimuthal direction; total wall shear stress at the plate surface

INTRODUCTION

The nature of bulk flow induced in the cone–plate viscometer affects both the interactions of particles placed in suspension in this device, and the shear stress applied on the plate surface. Exploiting these features of flow, researchers in the biomedical/biophysical sciences have used the cone–plate viscometer to study both cell-surface receptor function and shear-induced cellular activation phenomena. For example, the viscometer has been used to assess homotypic neutrophil adhesion rates in suspension (Neelamegham et al., 1997, 1998; Taylor et al., 1996). In these studies, experimental results were combined with mathematical analysis based on Smoluchowski's theory (Smoluchowski, 1917) to quantify the role of shear forces in controlling the function of adhesion molecules belonging to the L-selectin and β_2-integrin family. In other studies, the role of shear forces in inducing platelet activation has been measured by subjecting platelets in suspension to a range of shear rates in the viscometer (Goto et al., 1998; Moake et al., 1988), followed by biochemical analysis of cell-surface, intracellular, and secreted markers (see Kroll et al., 1996 for review). The role of shear forces in altering the function of surface-adherent cells, including endothelial and smooth muscle cells, has also been studied by anchoring cells on the plate surface of the viscometer and applying shear fields by rotation of the cone (Dewey, 1984; Ohno et al., 1993; Wagner et al., 1997).

The assumption made in biological literature, that flow is uniform and linear in the cone–plate viscometer, is violated at the higher shear rates. Indeed, at low shear rates the flow in the viscometer is in one dimension. There is only a rotational velocity component, which varies linearly with distance from the plate surface. This flow is termed as "primary flow." Although this is valid for low shear rates, at high shear rates, centrifugal forces cause an outward radial motion of the fluid near the rotating cone surface and an inward radial flow near the plate. This additional radial motion of the liquid is called "secondary flow" (Savins and Metzner, 1970; Sdougos et al., 1984). We have recently shown that, in the range of shear rates typically used in biological experiments, significant nonlinear secondary flow exists in the viscometer (H. Shankaran and S. Neelamegham, submitted for publication). The extent of secondary flow depends upon the cone angle, α, and the flow Reynolds number, Re ($= R^2 \Omega / v$) (Fewell and Hellums, 1977; H. Shankaran and S. Neelamegham, submitted for publication). In this work, we also showed that secondary flow causes a three-dimensional flow pattern in the viscometer and it results in: 1) positional variations in the velocity gradient, inter-particle forces, collision frequencies, and attachment times within the viscometer, 2) the application of unusually high shear forces at the edge of the plate surface, and 3) the application of time-varying hydrodynamic shear stresses on particles circulating in suspension.

In the current manuscript, we discuss possible implications of secondary flow on measurements of cellular aggregation, platelet activation, and endothelial cell mechanotransduction in the viscometer. In particular, we present a deterministic approach to model cellular aggregation under nonlinear/secondary flow conditions. The model distinguishes between the contributions of the hydrodynamic

flow parameters such as interparticle forces and attachment times, and the kinetic parameters that regulate receptor–ligand bond formation rates. The existence of positional variations in the hydrodynamic flow features due to secondary flow suggests that cellular aggregation rates in suspension may also vary with position. To verify these theoretical predictions in an experimental system, we examined the case of L-selectin and β_2-integrin-mediated neutrophil homotypic aggregation (Taylor et al., 1996). We observed that increasing Re by increasing the sample volume at a constant shear rate both decreased the cell adhesion kinetics and augmented the disaggregation rates. The experimental results are consistent with our theoretical prediction of secondary flow in the viscometer. Our analysis of neutrophil homotypic aggregation provides new insight into the biophysical features that regulate selectin- and integrin-mediated adhesion. Further, the theoretical framework applied here to examine cell aggregation in the cone–plate viscometer may be extended to examine cell aggregation mechanics for other three-dimensional or nonlinear flows.

METHODS

Mathematical modeling of flow and particle interactions

Primary and secondary flow in the viscometer

The cone–plate viscometer consists of a stationary plate placed below an inverted rotating cone of angle, α (Fig. 1). In typical biological experiments, the cone is rotated at a constant angular velocity, Ω. At low angular velocities, flow in a cone–plate viscometer has only a rotational velocity component about the cone axis. This velocity in the rotational ϕ direction is denoted w. The velocities in the radial r direction, u, and the vertical θ direction, v, are both zero. This type of flow is termed as primary flow. During primary flow, the velocity w increases linearly between the plate and the cone with increasing angle from the plate surface, β (Fig. 1). The
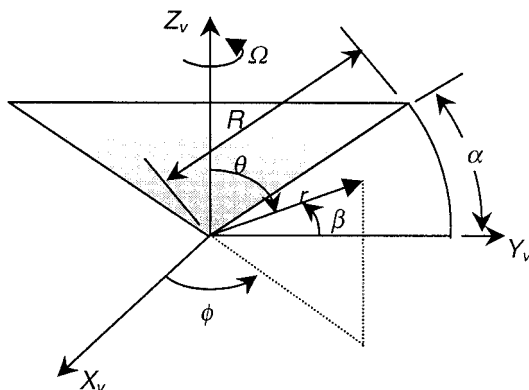

FIGURE 1 Coordinate system for flow in a cone–plate viscometer. Figure depicts schematic of a cone–plate viscometer with cone angle α and radius R. In the cartesian coordinate system, Z_v coincides with the cone axis, and X_v and Y_v lie on the plate surface. The spherical coordinate system is defined by the axes (r, θ, ϕ). Ω is the angular velocity of the cone about Z_v. The angle β is defined as $\pi/2 - \theta$. β varies from 0 at the plate surface to α at the cone surface.

velocity gradient tensor at a radial distance r and angle β under primary flow can be written in spherical coordinates for small cone angles as

$$\mathbf{G} = \begin{bmatrix} 0 & 0 & 0 \\ 0 & 0 & -(1/r)(\partial w/\partial \beta) \\ 0 & 0 & 0 \end{bmatrix}. \quad (1)$$

For small cone angles, the nonzero term in the velocity gradient tensor, $G_{(23)}$ $(= -1/r\,(\partial w/\partial \beta))$, can be written as Ω/α, and, hence, primary flow can be approximated to be a simple shear flow with a shear rate of Ω/α (/s). Ω/α is abbreviated as G, the primary flow shear rate, and it is independent of position in the viscometer. This approximation that flow in the cone–plate viscometer is equivalent to simple shear flow is used in most studies that examine biological phenomena.

Secondary flow results when the cone angle and angular velocity of the rotating cone are increased. This additional flow occurs under conditions when significant centrifugal forces push the liquid radially out near the cone surface. The requirement of continuity causes a radial inward motion near the plate surface, thereby setting up fluid circulation. Thus, all the velocity components (u, v, and w) are nonzero, and they vary with position in the viscometer. Also, these velocity components do not vary in the ϕ direction because the flow is rotationally symmetric (i.e., $\partial/\partial \phi$ terms are set to zero). The complete velocity gradient tensor $\mathbf{G}$ for the flow under these conditions, is written in spherical coordinates as

$$\mathbf{G} = \begin{bmatrix} \dfrac{\partial u}{\partial r} & \dfrac{\partial v}{\partial r} & \dfrac{\partial w}{\partial r} \\ -\dfrac{1}{r}\dfrac{\partial u}{\partial \beta} - \dfrac{v}{r} & -\dfrac{1}{r}\dfrac{\partial v}{\partial \beta} + \dfrac{u}{r} & -\dfrac{1}{r}\dfrac{\partial w}{\partial \beta} \\ -\dfrac{w}{r} & -\dfrac{w\tan\beta}{r} & \dfrac{u}{r} + \dfrac{v\tan\beta}{r} \end{bmatrix}. \quad (2)$$

As seen, all nine components of $\mathbf{G}$ are nonzero. Further, because the individual velocity components (u, v, and w) vary nonlinearly with position in the viscometer, the velocity gradient tensor also varies with spatial coordinates.

In a previous analysis, a numerical solution of the detailed primary and secondary flow in the cone–plate viscometer was obtained by solving the Navier–Stokes equation using finite difference methods (Fewell and Hellums, 1977; H. Shankaran and S. Neelamegham, submitted for publication). In this analysis, the (i, j)th grid point is defined to be located at (r_i^*, β_j). Here, $r_i^* = r_i/R$ is the dimensionless radial distance to the ith radial node, where R is the radial distance to the edge of the sample. Thus r_i^* is 0 at the cone apex and 1 at the edge of the sample. The vertical position of the jth vertical finite-difference node is denoted as β_j, which varies from 0 at the plate surface to the cone angle α at the cone surface. The numerical analysis indicated that the important parameters that regulate flow in the device are the cone angle, α, and the dimensionless flow Reynolds number, Re,

$$\text{Re} = \frac{R^2 \Omega}{v}. \quad (3)$$

Here, v is the kinematic viscosity of the fluid. For our current analysis, we calculated the flow velocities (u, v, and w) at each position (r_i^*, β_j) of the finite difference grid for a range of flow conditions (H. Shankaran and S. Neelamegham, submitted for publication). Once the flow velocities were obtained, the local velocity gradient tensor $\mathbf{G}$ (Eq. 2) was also evaluated at each position in the viscometer.

Estimating wall shear stress at the plate surface

The velocity gradient $\mathbf{G}$ for flow can be broken up into the rate-of-strain tensor $\mathbf{S}$ and the vorticity tensor $\mathbf{\Lambda}$, which represent the extensional and rotational components of the local flow field according to Aris (1989),

$$\mathbf{G} = \mathbf{S} + \mathbf{\Lambda}. \qquad (4)$$

The rate of strain tensor $\mathbf{S}$ for the flow is expressed as $\mathbf{S} = \frac{1}{2}(\mathbf{G} + \mathbf{G}^T)$ and the vorticity tensor $\mathbf{\Lambda}$ as $\mathbf{\Lambda} = \frac{1}{2}(\mathbf{G} - \mathbf{G}^T)$, where $\mathbf{G}^T$ is the transpose of $\mathbf{G}$. The elements of the tensor $\mathbf{S}$ evaluated at the plate surface provide information on the wall shear stress. The wall shear stress in the azimuthal (rotational, ϕ) and radial (r) directions can be expressed as $\tau_\phi = 2\mu S_{(32)}$ and $\tau_r = 2\mu S_{(13)}$. The total shear stress at the wall is given as $\tau_{\text{tot}} = (\tau_r^2 + \tau_\phi^2)^{1/2}$. In our analysis, numerically obtained velocity gradient tensor $\mathbf{G}$ was used to calculate the total wall shear stress at the plate surface at various radial distances from the cone apex.

Interparticle collision frequency in nonlinear flow

Collision frequency (number of collisions/m³/s) is a function of the local fluid velocity gradient $\mathbf{G}$, the particle concentration, and particle size. In our analysis, we assume that the sheared fluid consists of a suspension of spherical particles of radius r_P bearing surface microvilli of length λ. Particles are also assumed to follow a linear trajectory prior to collision, and the particle concentration (N_P) is assumed to be constant throughout the viscometer. When such particles collide, it is possible to imagine a spherical surface called the "collision sphere" with radius $2(r_P + \lambda)$ centered around one of the spheres. It is seen that, if the center of any other particle passes through this collision sphere, collision between the particles will occur. Our approach is to calculate the collision frequency by estimating the total mass transfer rate C_P, of particles into the collision sphere,

$$C_P = - \iint\limits_{\text{collision sphere}} N_P \mathbf{n} \cdot \mathbf{u}_c \, dA, \qquad (5)$$

where dA is an area element on the surface of the collision sphere, $\mathbf{n}$ is a unit normal vector directed out of this element, and $\mathbf{u}_c$ is the relative velocity between the centers of the colliding spheres. The relative velocity vector $\mathbf{u}_c$ can be written as $\mathbf{u}_c = \mathbf{r}_c \cdot \mathbf{G}$ (Aris, 1989), where $\mathbf{G}$ is from Eq. 2 and $\mathbf{r}_c$ is the position vector of the area element on the collision sphere. The negative sign on the right-hand side of Eq. 5 accounts for the direction of mass transfer. Thus, mass transfer into the sphere results in a positive C_P value and vice versa. To evaluate the double integral (Eq. 5) over the entire surface of the collision sphere, the collision sphere was divided into a series of discrete area elements as described elsewhere (H. Shankaran and S. Neelamegham, submitted for publication) and the mass flux into the collision sphere was summed over all elements. C_P obtained in this fashion was multiplied by $N_P/2$ to estimate the local collision frequency $C(r_i^*, \beta_j)$ per unit volume evaluated at each point (r_i^*, β_j) in the viscometer, i.e., $C(r_i^*, \beta_j) = N_P/2 \cdot C_P$. The factor of $\frac{1}{2}$ is introduced to prevent double counting of particles.

In our simulations, we used the numerically computed flow gradients (Eq. 2) to calculate the collision frequency $C(r_i^*, \beta_j)$ at each grid point in the viscometer. A volume-averaged collision frequency, $\bar{C}$ for the entire viscometer was then computed using the expression

$$\bar{C} = \frac{\displaystyle\sum_{i=1}^{M}\sum_{j=1}^{N} C(r_i^*, \beta_j)\Delta V(r_i^*, \beta_j)}{\displaystyle\sum_{i=1}^{M}\sum_{j-1}^{N} \Delta V(r_i^*, \beta_j)}, \qquad (6)$$

where $\Delta V(r_i^*; \beta_j)$ is the volume of the element centered around the point $(r_i^*; \beta_j)$ in the viscometer.

Doublet interactions: interparticle forces for a rigid dumbbell

We examined two-body interactions for particles subjected to secondary flow. Fluid inertial terms were neglected in this analysis because the contribution is small (Aidun et al., 1998), and the particle hydrodynamics are assumed to be Stokesian. Previously, such analysis, when performed on particles subjected to simple linear shear, yielded analytical expressions for interparticle forces (Eqs. 34 and 35 in Tha and Goldsmith, 1986) and doublet rotational trajectories (Eqs. 46 and 47 in Arp and Mason, 1977) in terms of the shear rate, G. Whereas the previous analysis of simple shear considered a flow gradient with only one nonzero component, our case of secondary flow is more complex with nine nonzero terms in the flow gradient. Due to this complexity and the positional variations in the flow gradient within the viscometer, it is not possible to express forces and trajectories in a concise analytical fashion as a function of Reynolds number and cone angle.

The detailed methodology for computing interparticle forces and trajectories is presented in H. Shankaran and S. Neelamegham (submitted for publication) based on work by Brenner and O'Neill (1972) and Arp and Mason (1977). The coordinate systems used for the calculation are described in Fig. 1 of Arp and Mason (1977). Briefly, this analysis considers two sets of orthogonal axes, both with coincidental origins midway between the colliding species. One of the coordinates, called space-fixed coordinates (X_i), is with respect to the macroscopic flow coordinates (r, θ, ϕ) of the viscometer. The orientation of any doublet is described by two angles (θ_1, ϕ_1), which are spherical polar and azimuthal angles with respect to the space-fixed axis X_1. The second system, known as the particle-fixed coordinates (X_i') is with respect to the interacting particles with one of the axes (X_3') passing through the center of both the interacting particles. The calculation methodology involves transformation of the velocity gradient tensor, $\mathbf{G}$, expressed in space-fixed coordinates (Eq. 2), into particle-fixed coordinates to obtain the tensor $\mathbf{G}'$. The fluid velocity vector $\mathbf{u}_f'$ is then obtained in particle-fixed coordinates. The rate-of-strain tensor for the fluid is calculated in particle-fixed coordinates using the expression $S' = \frac{1}{2}(\mathbf{G}' + \mathbf{G}'^T)$. The interparticle normal force, $F_{(3)}'(\theta_1, \phi_1)$ applied between the colliding species oriented at (θ_1, ϕ_1) can then be obtained using the following equation (see H. Shankaran and S. Neelamegham, submitted for publication, for derivation),

$$F_{(3)}'(\theta_1, \phi_1) = - \mu((f + 2g)S_{(33)}' - bu_{f(3)}'), \qquad (7)$$

where μ is the viscosity of the fluid, and b, f, and g are force/torque coefficients for interaction between a pair of smooth spheres. The force/torque coefficients are functions of the size of the spheres (r_P) and the separation distance between them (2λ) as tabulated elsewhere (Table I in Arp and Mason, 1977). In our analysis of the normal force experienced by rigid dumbbells, we calculated $F_{(3)}'$ for all possible doublet orientations ($0 \leq \theta_1 \leq \pi$, and $0 \leq \phi_1 \leq 2\pi$) at the different grid points in the viscometer using the numerically computed values of the local flow gradient $\mathbf{G}$. For each point, we then determined the maximum normal force, $F_{\max}(r_i^*, \beta_j)$ using the definition,

$$F_{\max}(r_i^*, \beta_j) = \text{Max}[F_{(3)}'(\theta_1, \phi_1)]; \quad 0 \leq \theta_1 \leq \pi;$$

$$0 \leq \phi_1 \leq 2\pi. \qquad (8)$$

$F_{\max}(r_i^*, \beta_j)$ is a local parameter that depends on position in the device. These $F_{\max}(r_i^*, \beta_j)$ values were weighted by the number of interparticle collisions at each point, and averaged to obtain the collision-averaged

maximum normal force, $\bar{F}_{\max}$ for the entire viscometer by using the expression

$$\bar{F}_{\max} = \frac{\displaystyle\sum_{i=1}^{M}\sum_{j=1}^{N} F_{\max}(r_i^*, \beta_j) C(r_i^*, \beta_j) \Delta V(r_i^*, \beta_j)}{\displaystyle\sum_{i=1}^{M}\sum_{j=1}^{N} C(r_i^*, \beta_j) \Delta V(r_i^*, \beta_j)}. \qquad (9)$$

Therefore, a rigid particle doublet in a viscometer, formed upon interparticle collision, would, on an average, experience a maximum breakup force of $\bar{F}_{\max}$.

Doublet interactions: rotation of a rigid dumbbell

In our analysis, we assume that, after collision, the particle doublets behave as rigid dumbbells that rotate in the flow field. The rotational trajectory of the rigid dumbbell formed following collision can be expressed by the following equations in space-fixed coordinates (H. Shankaran and S. Neelamegham, submitted for publication),

$$\frac{d\phi_1}{dt} = \mathbf{\Omega}_{S(1)} - \frac{\cos\theta_1}{\sin\theta_1} [\cos\phi_1 \mathbf{\Omega}_{S(2)} + \sin\phi_1 \mathbf{\Omega}_{S(3)}], \quad (10)$$

$$\frac{d\theta_1}{dt} = \mathbf{\Omega}_{S(3)} \cos\phi_1 - \mathbf{\Omega}_{S(2)} \sin\phi_1, \qquad (11)$$

where $\mathbf{\Omega}_{S(i)}$ are components of the vector $\mathbf{\Omega}_S$, the rotational velocity vector for the rigid dumbbell expressed in space-fixed coordinates. $\mathbf{\Omega}_S$ can be computed based on the orientation of the dumbbell and the velocity gradient tensor $\mathbf{G}$. Thus, to obtain the rotational trajectory of a rigid dumbbell at any given point in the viscometer, Eqs. 10 and 11 are solved numerically with $\mathbf{\Omega}_S$ being calculated at each time step as a function of dumbbell orientation.

Cellular aggregation in the viscometer

Model formulation and assumptions

In this section, we present the conceptual framework and the assumptions involved in our model for cell aggregation in the cone–plate viscometer. The process of aggregation under flow is modeled as involving two sequential steps: cell–cell collision caused by the relative motion of particles in suspension, and cell adhesion at a certain rate. The rate of particle collision is estimated using the analysis presented in the previous section (Eqs. 5 and 6). After collision, the doublet formed is assumed to behave as a rigid dumbbell that rotates in the flow field (Tha et al., 1986). The force felt along the line joining the centers of the colliding species is initially compressive (Eq. 7), and it tends to push the cells toward each other.

Receptor–ligand bond formation between interacting cells commences immediately after particle collision, and the net rate of bond formation is presumably high, because, on average, the bonds are not stressed by the hydrodynamic flow field. As the particle doublet continues to rotate, beyond a particular orientation the net force experienced by the doublet changes from a compressive to a tensile force. The tensile forces pull the cells away from each other. These forces tend to exert stresses on receptor–ligand bonds and augment bond breakage. Eqs. 12a and 12b below, based on previously published deterministic kinetic models (Bell, 1978; Hammer and Lauffenburger, 1987), describe the evolution of intercellular bonds with time t during the compressive/attachment and tensile/detachment force zones, respectively. Here, N_b denotes the number of intercellular bonds formed.

$$\frac{dN_b}{dt} = k_f^0 N_L (R_T - N_b) - k_r^0 N_b, \qquad (12a)$$

$$\frac{dN_b}{dt} = k_f^0 N_L (R_T - N_b) - [k_r^0 \exp(\gamma F'_{(3)}/k_b T N_b)] N_b, \qquad (12b)$$

where, k_f^0 is the forward rate (m²/s), k_r^0 is the intrinsic zero-force reverse rate (/s), N_L is the density of ligands in the intercellular contact area that may form bonds with the receptor (/m²), R_T is the number of receptors on the surface of the cell, γ is the bond interaction parameter (m), k_b is the Boltzmann constant (J/K), T is the temperature (K), and $F'_{(3)}$ is the total tensile force (N) along the line joining the centers of the interacting cells. It should be noted that, in the above equation, R_T represents the number of receptors per cell, and that the equations are written in a generalized form for bond formation between receptors on the first cell and complementary ligands on the second cell. If the two interacting cells are identical, the above equations can still be used to describe bond formation. However, the forward rate, k_f^0 in this case, would be equal to twice the intrinsic forward rate for the interacting receptor–ligand pair, because the same set of receptors and ligands would be present on both the cells.

For any cell–cell collision to result in stable aggregate formation, the number of receptor–ligand bonds should be greater than the critical number of bonds (N_b^{crit}) required to withstand the applied tensile force at all times. The critical number of bonds is defined as the ratio of the total tensile force $F'_{(3)}$ to the bond strength f_c(N). For a doublet to remain stably aggregated during the tensile/detachment phase, it must therefore satisfy the criterion,

$$N_b > N_b^{\mathrm{crit}}, \quad \text{where} \quad N_b^{\mathrm{crit}} = \frac{F'_{(3)}}{f_c}. \qquad (13)$$

This criterion is similar to the one used by Tandon and Diamond (1998, Eq. 3) in a previous model of cell aggregation. In our analysis, we assume the bond strength f_c to be 100 pN (Table 1). In reality, the bond strength is a dynamic quantity, which depends on the rate of loading (Evans and Ritchie, 1997). For the range of loading rates encountered by a rotating doublet, it is thought that a bond strength of 100 pN is a reasonable value.

The following simplifying assumptions are made in our model for cell aggregation: 1) The model is restricted to the analysis of doublets of

TABLE 1 Parameters used for modeling neutrophil aggregation

Parameter	Value*	Reference
Receptor number (R_T)	80,000	Simon et al., 1992; Taylor et al., 1996
Intrinsic reverse rate (k_r^0)	5/s	Puri et al., 1998; Schmidtke and Diamond, 2000
Bond interaction parameter (γ)	0.02 nm	Puri et al., 1998
Bond strength (f_c)	100 pN	Tandon and Diamond, 1998
Neutrophil radius[†]	3.7 μm	Neelamegham et al., 1997
Microvilli length[†]	0.4 μm	Shao et al., 1998

*Same values used for selectin-limited and integrin-limited regimes.

[†]These parameters are used to evaluate the interparticle forces and doublet trajectories.

equal-sized particles, although it could be extended to unequal-sized particles or multi-particle interactions. This simplified approach, which examines only singlet–singlet interactions, is thought to be valid while modeling neutrophil aggregation rates during the first 60 s after the application of shear. This is because, in our experiments, the number of doublets formed during this time was ~5 times more than aggregates of any other size (Neelamegham et al., 1997, 2000). Further, the volume occupied by the cells was small (volume fraction ~10^{-4}), thus making multi-particle interactions unlikely. 2) While modeling neutrophil aggregation kinetics, the neutrophils are treated as uniform smooth spheres with a radius of 3.7 μm. Also, after collision, the cells composing the doublet are assumed to be separated by a distance equal to twice the length of the microvilli (= 0.8 μm) (Shao et al., 1998). Although this is not strictly true, we make this assumption as a model approximation. In reality, neutrophils are not all identical, and, after cell–cell contact, the extent of interdigitation is likely to change with time. 3) In calculating interparticle interactions, the doublet is assumed to be subjected to a time-invariant velocity gradient, which depends on the coordinates in the viscometer where particle collision occurs. At high shear rates, secondary flow causes radial fluid circulation in the viscometer, and variations in the velocity gradient with radial position in the device. However, our assumption of a constant velocity gradient during doublet interaction is justified, because the time-scale of doublet interactions is ~2–3 orders of magnitude smaller than the time scale of fluid motion in the radial direction induced by secondary flow (H. Shankaran and S. Neelamegham, submitted for publication). 4) In modeling the role of hydrodynamic forces in modulating cell aggregation, only the normal force component is considered. In reality, receptor–ligand bonds are subjected to both shear forces (tangential to the surface of the cell) and normal forces (along the line joining the centers of the cells). Because the normal force is ~3 times larger than the shear force at all times (H. Shankaran and S. Neelamegham, submitted for publication), we consider this component to be more important in modulating bond formation. Further, we assume that the tensile force is distributed evenly over all receptor–ligand bonds (i.e., force per bond = net tensile force/number of bonds). This is in spite of the fact that all intercellular bonds are not oriented identically on the surface of the cell or microvilli.

Modeling the kinetics of homotypic neutrophil aggregation

Homotypic neutrophil aggregation is a complex process involving interactions between multiple receptors and ligands. The three important sets of receptors involved are the L-selectin molecule and the β_2-integrin subunits, LFA-1 and Mac-1 (Taylor et al., 1996). Among the ligands identified to date, L-selectin has been shown to bind PSGL-1 and other homologous ligands (Guyer et al., 1996), LFA-1 binds ICAM-3 and other ligands (Neelamegham et al., 2000), and the ligand(s) for Mac-1 is yet unidentified. Several studies have suggested that changes in the expression level, distribution, and affinities of these receptor–ligand pairs with time after stimulation may control neutrophil adhesion rates (Kishimoto et al., 1989; Springer, 1995). In the first 30 s after 1μM formyl peptide (fMLP) stimulation, we have observed less than a 15% change in expression level of L-selectin and β_2-integrin (Taylor et al., 1996). However, by 10 min, L-selectin expression in isolated neutrophils falls by ~85% and there is an ~10 fold increase in β_2-integrin levels.

Fluid flow may also alter the biophysics of neutrophil aggregation through a variety of mechanisms. Increasing the shear rate during neutrophil aggregation causes an increase in the force applied on receptor–ligand bonds, thus presumably augmenting the breakage of existing bonds. In addition, at low shear rates below ~400/s, increasing the shear rate causes a counter-intuitive increase in L-selectin-mediated adhesion rates (Taylor et al., 1996). Based on studies in other experimental systems (Finger et al., 1996; Lawrence et al., 1997), this augmentation of L-selectin-mediated adhesion with shear has been termed the "threshold" phenomenon of L-selectin. Potential mechanisms for the threshold phenomenon include: 1) an extension in neutrophil microvilli length with shear, leading to a

reduction in applied forces on receptor–ligand bonds (Schmidtke and Diamond, 2000; Shao et al., 1998), 2) increase in the encounter rate between receptors and ligands due to an increase in the relative velocity between cells (Chang and Hammer, 1999; Chen and Springer, 1999; Finger et al., 1996), 3) increase in cell deformation and a consequent increase in the contact area between interacting cells at higher shears (Lawrence et al., 1997), 4) higher rates of receptor/ligand diffusion into the adhesive contact zone due to increased membrane fluidity (Haidekker et al., 2000), 5) increased bond formation kinetics due to either the nature of bond loading, or the ability of shear forces to surmount energy barriers that otherwise limit receptor–ligand bond formation (Evans and Ritchie, 1997; Merkel et al., 1999). In addition, with regards to the origin of the threshold phenomenon, it has been shown that chemical modification of the L-selectin ligand abrogates this phenomenon (Puri et al., 1998). This might potentially be due to a redefinition of the energy landscape for receptor–ligand interactions in the system.

As seen, homotypic neutrophil aggregation is mediated by a variety of sequential or parallel binding events, which provide a set of checks and balances to control cell binding rates. Although a previous model of neutrophil aggregation considered two sets of parameters to account for the contributions of L-selectin and β_2-integrin (Tandon and Diamond, 1998), our approach uses a single set of parameters. The objective is to limit the number of model-fitted parameters, because inclusion of additional parameters would increase the complexity of the model while still only providing a phenomenological description for the aggregation system. Further, based on the above discussion, because a myriad of biological and transport features regulate the rate of receptor–ligand interaction and their binding, we treat the quantity $k_f^0 N_L$ (/s), as a lumped on-rate parameter for bond formation. This parameter implicitly contains information about the forward rate of bond formation, the contact area between the interacting cells, the number of ligands on the cell surface, and the rate at which ligands diffuse into the contact area.

Our treatment of the cell aggregation process is based on our experimental observations (Taylor et al., 1996; Neelamegham et al., 1997). At low shear rates (G ~ 100/s), neutrophil aggregation is rate-limited by the kinetics of β_2-integrin bond formation, because addition of an anti-L-selectin antibody does not alter the adhesion efficiency (Taylor et al., 1996). Further, at this shear rate anti-β_2-integrin antibodies completely abolish neutrophil aggregation. At higher shear rates (especially $G >$ 400/s) the aggregation process is selectin-limited because blocking with the anti-L-selectin antibody completely abrogates cell adhesion. This part of the model implicitly assumes that, if sufficient L-selectin bonds are formed in the first orbit after collision to sustain the transient aggregate, stable aggregation mediated by β_2-integrin will eventually result. This appears to be a reasonable assumption, because formation of a few L-selectin bonds in the first orbit will allow time for additional integrin and selectin bond formation. In our model, depending on the shear rate being examined, the parameters R_T and $k_f^0 N_L$ correspond to the receptor and ligand pair that are rate limiting. Hence, at low shear, R_T corresponds to the number of β_2-integrins and $k_f^0 N_L$ captures the features of the ligands of the integrins. At higher shear rates, R_T corresponds to the L-selectin molecules and $k_f^0 N_L$ corresponds to the selectin-ligands. The kinetic parameters are thus assumed to be representative of the overall nature of the binding process, rather than being the actual biophysical properties for a single type of receptor–ligand pair. Because the number of L-selectin and β_2-integrin molecules is similar (Simon et al., 1992; Taylor et al., 1996), R_T is set to 80,000 for both L-selectin and β_2-integrin regardless of the shear rate (Table 1). The other unknown parameters in the kinetic equation (Eq. 1) are k_r^0, γ, and $k_f^0 N_L$. Some of these parameters were obtained based on published data for L-selectin- and β_2-integrin-mediated interactions and are listed in Table 1. These values are kept constant over the entire range of shear rates and sample volumes used in our simulations. As a note to the reader, γ and k_r^0 are included in this paper for the sake of complete model formulation, but they do not markedly affect the simulation results presented here. Also, because several adhesion features are thought to increase with shear rate and contribute to the threshold phenomenon, we have varied

the lumped on-rate $k_f^0 N_L$ with shear rate (G) to model the increased level of L-selectin-mediated adhesion. It is thought that these assumptions are reasonable given that the primary focus of this manuscript is on the contribution of secondary flow. Should a more definite mechanism be identified in the future to account for the threshold phenomenon, appropriate changes may be made to the deterministic model.

Adhesion efficiency

To quantify the contribution of secondary flow to cell adhesion kinetics, we estimate a parameter known as the adhesion efficiency. This is evaluated both locally at each grid point in the viscometer, $\eta(r_i^*, \beta_j)$, and globally over the entire volume of the device, $\bar{\eta}$.

The local adhesion efficiency $\eta(r_i^*, \beta_j)$ is defined as the probability of a cell collision resulting in stable aggregate formation at the position (r_i^*, β_j),

$$\eta(r_i^*, \beta_j) = \frac{\text{Number of collisions resulting in adhesion at } (r_i^*, \beta_j)}{\text{Total number of collisions at } (r_i^*, \beta_j)}. \quad (14)$$

For local adhesion efficiency computations, N_{col} weighted-random initial collision orientations were generated at each of the grid points of the cone–plate viscometer. The initial collision orientations were computed based on the expression for the fractional number of collisions (dC_P) at any given collision orientation (θ_1, ϕ_1) in area element (dA) on the collision sphere (Eq. 5). Normalization of dC_P with the overall local collision frequency, $C(r_i^*, \beta_j)$ yielded a distribution function that described the variation in the frequency of collision with particle collision orientation. In our computations, this distribution function was generated for each node in the viscometer. Based on the distribution function, we then generated a similar pattern of weighted random numbers using an IMSL™ (Visual Numerics Inc., Houston, TX) routine RNGCS (Akima, 1970; Guerra et al., 1976). These weighted-random numbers were then used to obtain N_{col} number of collision orientations at each node point in the viscometer. Each of these collision orientations was denoted as $(\theta_1^0, \phi_1^0)_k$, where k varies from 1 to N_{col}.

For each collision orientation, the possibility that the collision would result in stable aggregate formation was then evaluated using the bond formation and particle interaction model (Eqs. 7, and 10–12) with initial conditions $N_b = 0$, and initial orientation $(\theta_1, \phi_1) = (\theta_1^0, \phi_1^0)_k$. For these calculations, because the forces are initially compressive, Eqs. 10, 11, and 12a were solved simultaneously for the first time step using the Petzold–Gear BDF method to determine the number of bonds formed and the new doublet orientation. The hydrodynamic force $F'_{(3)}$ (Eq. 7) was then evaluated based on the particle orientation. This force was used to choose between Eqs. 12a (for the compressive/attachment phase) and 12b (for the tensile/detachment phase), and to update the $F'_{(3)}$ parameter in Eq. 12b, if necessary. Eqs. 10–12 were again solved for the next time step. This process was repeated at each time increment to calculate the number of inter-particle bonds and corresponding collision orientation until the doublet either left the tensile zone, i.e., the detachment phase and re-entered the compressive force zone, or failed to satisfy the criterion in Eq. 13, whichever occurred first. Whereas the former situation implies stable aggregate formation, the latter corresponds to aggregate break-up and thus an unsuccessful collision. The analysis was repeated for all N_{col} collisions using the respective initial collision orientations, and the number of successful collisions was counted. The local adhesion efficiency, $\eta(r_i^*, \beta_j)$, was then evaluated at the node point (r_i^*, β_j) according to Eq. 14. The calculation was performed for all the grid points in the viscometer.

The overall adhesion efficiency for the entire viscometer is a weighted-average of the local adhesion efficiency based on the number of collisions occurring in each region of the device. One way of calculating this parameter is to determine the local adhesion efficiencies for all the $M \times N$

grid points in the viscometer as described above, and averaging them using the equation

$$\bar{\eta} = \frac{\sum_{i=1}^{M} \sum_{j=1}^{N} \eta(r_i^*, \beta_j) C(r_i^*, \beta_j) \Delta V(r_i^*, \beta_j)}{\sum_{i=1}^{M} \sum_{j=1}^{N} C(r_i^*, \beta_j) \Delta V(r_i^*, \beta_j)}, \quad (15)$$

where $C(r_i^*, \beta_j)$ and $\Delta V(r_i^*, \beta_j)$ are the local collision frequency and volume associated with the (r_i^*, β_j) node, respectively. For $M = 11$, $N = 15$, and $N_{col} = 1000$, this would require us to analyze 117,000 collisions. We found that this was a computationally intensive methodology, especially when estimates of overall adhesion efficiency were required for a range of conditions (e.g., over a range of Re and α). Accurate estimates of $\bar{\eta}$, presented here, were instead obtained by analyzing collisions occurring at different points in the viscometer by randomly generating collision coordinates, and thus sampling different areas of the device in a statistical fashion. Thus to calculate $\bar{\eta}$, 1000 random collision points were generated by using a weighting function based on the total number of collisions occurring in each region of the device. The weighting process ensured that regions with greater number of collisions were more likely to be chosen for the efficiency calculation. For each of these collision points, a weighted-random collision orientation was obtained as described previously for the local adhesion efficiency calculations. The bond formation and particle interaction model (Eqs. 7, 10–12) was then used to determine whether the collision resulted in stable aggregate formation. The overall adhesion efficiency $\bar{\eta}$ was then calculated as the ratio of the number of collisions resulting in stable aggregate formation to the total number of collisions considered (= 1000). The simulation was repeated five times with different random number seeds for generating the weighted-random collision coordinates, and the results were averaged to obtain an estimate for $\bar{\eta}$. It was seen that this mean adhesion efficiency obtained by analyzing 5000 collisions in all, deviated from $\bar{\eta}$ calculated using Eq. 15 by <3%.

Experimental determination of adhesion efficiency

Neutrophil homotypic aggregation studies

Neutrophil aggregation experiments were performed using established cone–plate viscometry methodology in a viscometer from Haake Inc. (Paramus, NJ) maintained at 37°C, followed by flow cytometric analysis of samples (Neelamegham et al., 1998, 2000). For these experiments, neutrophils were isolated from fresh human blood collected from healthy volunteers by venipuncture in 10 U heparin/ml anticoagulant as previously described (Taylor et al., 1996). The isolated neutrophils were kept at 4°C in Ca^{2+}-free HEPES buffer prior to experimentation. Before each experimental run, neutrophil suspensions at 10^6 cells/ml were placed in buffer containing 1.5 mM Ca^{2+} and stained with 10 ng/ml nuclear dye acridine orange for 3 min at 37°C. The cells were then placed in the gap between the cone and the plate, stimulated with 1 μM fMLP, and shear was applied. During the course of the experiment, 20-μl aliquots of the cell suspension were taken at fixed sampling time points for up to 5 min after stimulation. These samples were fixed in 200 μl of cold 0.5% paraformaldehyde solution containing 10 ng/ml acridine orange dye for flow cytometric analysis.

A FACSCalibur flow cytometer (Becton Dickinson, San Jose, CA) was used to analyze the particle distribution of fixed cell suspensions. The neutrophil population was identified by gating on their characteristic forward scatter versus side scatter. Singlet neutrophils and aggregates were resolved using green fluorescence derived from acridine orange staining, and the particle distribution of neutrophil aggregates was determined using histograms of fluorescence intensity. The extent of homotypic adhesion (%

Aggregation) was determined based on the rate of depletion of singlet neutrophils according to the equation

% Aggregation =

$$\left(1 - \frac{S}{S + 2D + 3Tr + 4Q + 5P + 6Sx}\right) \times 100, \quad (16)$$

where the neutrophil aggregate sizes are given by S = singlets, D = doublets, Tr = triplets, Q = quartets, P = pentuplets, and Sx = sextuplets and larger unresolved aggregates.

Estimating the adhesion efficiency of neutrophil homotypic aggregation

The details of the mathematical analysis used to estimate neutrophil homotypic adhesion efficiency have been published elsewhere (Hentzen et al., 2000; Neelamegham et al., 1997). Briefly, adhesion efficiency is estimated by fitting the aggregate size distribution data of homotypic neutrophil aggregation experiments over the first 60 s after the application of shear with a mathematical model. The total number of collisions is dependent on the cell concentration, applied shear rate, and cell radius, and it is estimated based on two-body linear collision theory. The number of effective collisions is then estimated based on the experimental aggregation data and the mathematical model.

Statistical analysis

Experimental data were analyzed using a paired t test to determine significance, and $p < 0.05$ was considered significant.

RESULTS

The effect of secondary flow on wall shear stress and particle interactions was studied. The role of secondary flow in modulating interparticle adhesion efficiency was also examined by calculating both local adhesion efficiencies and the overall collision-averaged efficiency at different values of cone angles and flow Reynolds numbers (Re). In our current theoretical analysis, α was varied from 0.009 to 0.035 radians (or ½ to 2°) and Re ranges from 0 to 1×10^5. These parameter values lie in the range of conditions observed in the typical biological experiments, where the shear rate varies from 0 to 10,000/sec and the cone angle varies from ⅓ to 2°. Theoretical predictions of adhesion efficiency obtained from our model were compared with experimental results to assess the contribution of secondary flow on neutrophil aggregation rates in the cone–plate viscometer.

Secondary flow alters the magnitude of shear stress on the plate surface

In experiments where cells (e.g., endothelial cells) are coated on the plate surface and subjected to fluid flow in the viscometer, the mechanical forces exerted on the plate due to hydrodynamic flow modify both the directional alignment (Dewey, 1984) and the biological properties of the cells (Ohno et al., 1993; Tsao et al., 1996). We examined

how secondary flow may affect the magnitude of wall shear stress at the plate surface. The numerically computed velocity gradient was used to compute the total shear stress (τ_{tot}) at different radial positions on the plate surface. These calculations were performed for a fixed shear rate (G) of 1000/s and a sample radius (R) of 25 mm (Fig. 2 A). For the cone angles of 0.5°, 1°, and 2° examined, the conditions correspond to Re values of 5454, 10,908, and 21,817, respectively. The sample volumes corresponding to R = 25 mm for cone angles of 0.5°, 1°, and 2° are 285, 571, and 1142 µl, respectively ($V = \frac{2}{3}\pi R^3 \tan \alpha$).

We observed that secondary flow causes an increase in the magnitude of the shear stress with radial position away from the cone vertex (Fig. 2 A). This is in contrast to primary flow where the wall shear stress is constant ($\tau = \mu G \sim \mu\Omega/\alpha$) and independent of radial position. In the case of a 0.5° viscometer, the wall shear stress did not deviate from the primary flow value. A sharp increase in shear stress was however observed at the outer edge of the viscometer for the cone angles of 1° and 2°. At Re = 10,908 for a 1° cone, the magnitude of shear forces applied at the periphery of the viscometer was ~1.6-fold that predicted by primary flow analysis. At Re = 21,817 for a 2° cone, the wall shear stress was ~5.1-fold that predicted by primary flow analysis at the radial edge of the viscometer. Based on these observations, we conclude that conditions that augment secondary flow also increase the applied wall shear stress.

Local collision frequency but not volume-averaged collision frequency is a strong function of secondary flow

The interpretation of particle aggregation data obtained from cone–plate viscometers requires an accurate model of the particle collision rates induced by the flow. Smoluchowski's two-body collision theory can be used to predict collision frequencies for primary flow where the velocity gradient has only one non-zero component (Evans and Proctor, 1978; Smoluchowski, 1917). This analysis predicts a constant collision frequency throughout the viscometer, which is given by collision frequency = $16/3 G N_P^2 (r_P + \lambda)^3$. The secondary flow velocity gradient $\mathbf{G}$, in contrast, varies with position in the viscometer and can have up to nine significant components (Eq. 2). Consequently, in this case, the collision frequency also may vary dramatically with position in the device. In support of this, our recent analysis indicated that the local collision frequency was up to ~5-fold higher than primary flow predictions, in certain regions near the edge of the viscometer at Re = 3×10^4 for a 2° cone-angle (H. Shankaran and S. Neelamegham, submitted for publication).

In spite of these local variations in collision frequency, the volume-averaged collision frequency for the entire viscometer was not markedly different from primary flow predictions (Fig. 2 B). Increasing secondary flow effects by increasing Re and the cone angle caused only modest
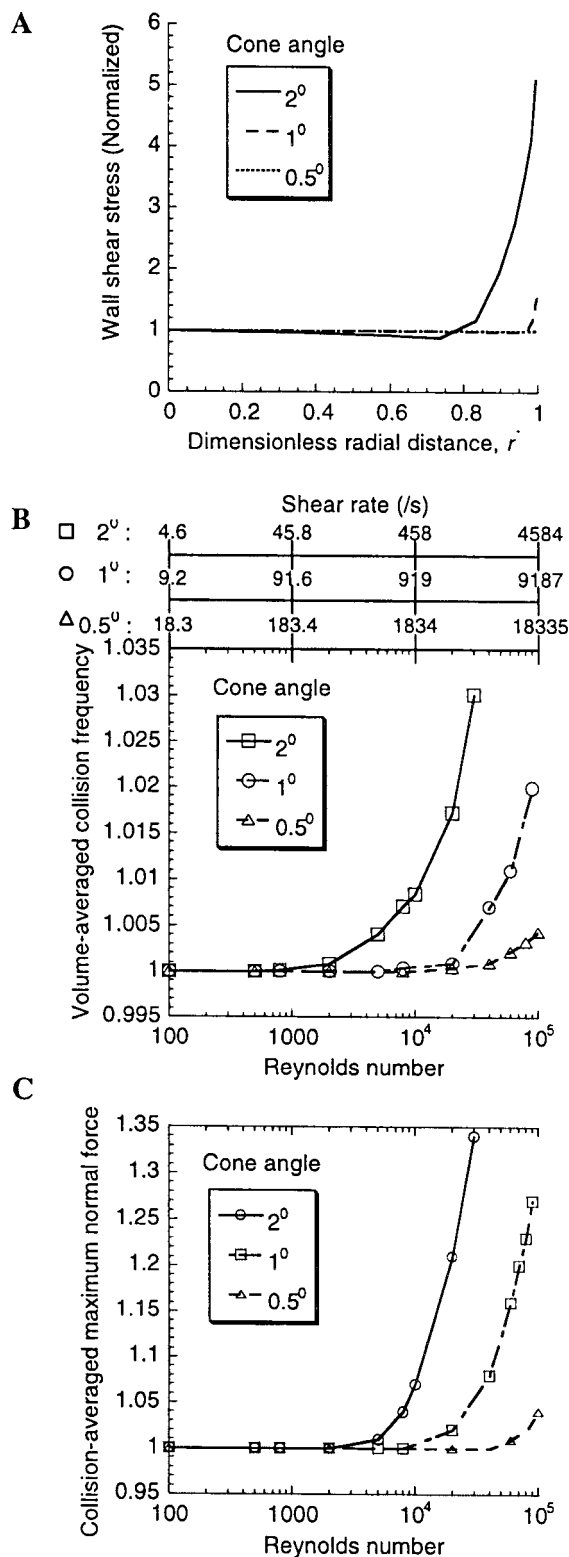
A

B

C

FIGURE 2 Wall shear stress and particle interactions under secondary flow. The numerically computed velocity gradient tensor was used to calculate the wall shear stress, collision frequency, and the magnitude of the interparticle normal force. These parameters were normalized with respect to their corresponding values under primary flow conditions. (*A*) Variation of normalized wall shear stress with radial position on the plate surface. Results are presented for a constant sample radius $R = 25$ mm and

changes ($\sim 3\%$) in the overall collision frequency. Apparently, in the range tested, although primary flow analysis is sufficient to predict the average collision frequency of particles in the viscometer, detailed secondary flow analysis is necessary to quantify positional variations.

Particle doublets experience increased forces under secondary flow conditions

In the case of primary flow, the maximum normal force is a linear function of shear rate G and is constant throughout the device (Tha and Goldsmith, 1986). Secondary flow however, caused positional variations in $F_{max}(r_i^*, \beta_j)$ within the viscometer (H. Shankaran and S. Neelamegham, submitted for publication). The nature of this variation was similar to that of the collision frequency. Here, too, we observed that the forces were up to 5-fold higher than primary flow predictions at certain regions near the radial edge of the sample. Unlike collision frequency, whose volume-averaged value for the entire viscometer did not change appreciably with Re and α, the collision-averaged maximum normal force $\bar{F}_{max}$ (Eq. 9) experienced by a doublet increased with these parameters (Fig. 2 *C*). A doublet suspended in a sample volume of 1.142 ml (sample radius = 25 mm) being sheared in a 2° viscometer at a shear rate of 1370/s was seen to experience a force which was, on average, $\sim 35\%$ higher than that predicted by primary flow analysis. In addition to the effect of secondary flow on the average normal force felt by a doublet in the viscometer, the existence of positional force variations could substantially change the local behavior of particles and the rate of particle binding in adhesion studies.

Stable aggregate formation depends upon attachment time and interparticle force

The extent of cell aggregation in suspension is a function of both kinetic and hydrodynamic parameters. The local velocity gradient in the fluid surrounding the interacting particles influences interparticle forces and attachment times. The attachment time is defined as the time the doublet spends in the compressive force regime prior to experienc-

shear rate $G = 1000$/s for three different cone angles. For the cone angles of 0.5°, 1°, and 2°, this corresponds to Reynolds numbers of 5454, 10,908, and 21,817, respectively. (*B*) Variation of volume-averaged collision frequency for the entire viscometer with flow Reynolds number and cone angle. The shear rate corresponding to each Re value is indicated on the top of the panel for the three different cone angles. The transformation from Re to shear rate is performed while assuming a fixed sample radius $R = 25$ mm. (*C*) Variation of collision-averaged maximum normal force for the entire viscometer with flow Reynolds number and cone angle. The transformation of Re to shear rate for this panel can be obtained using the axes shown on top of *panel B*.
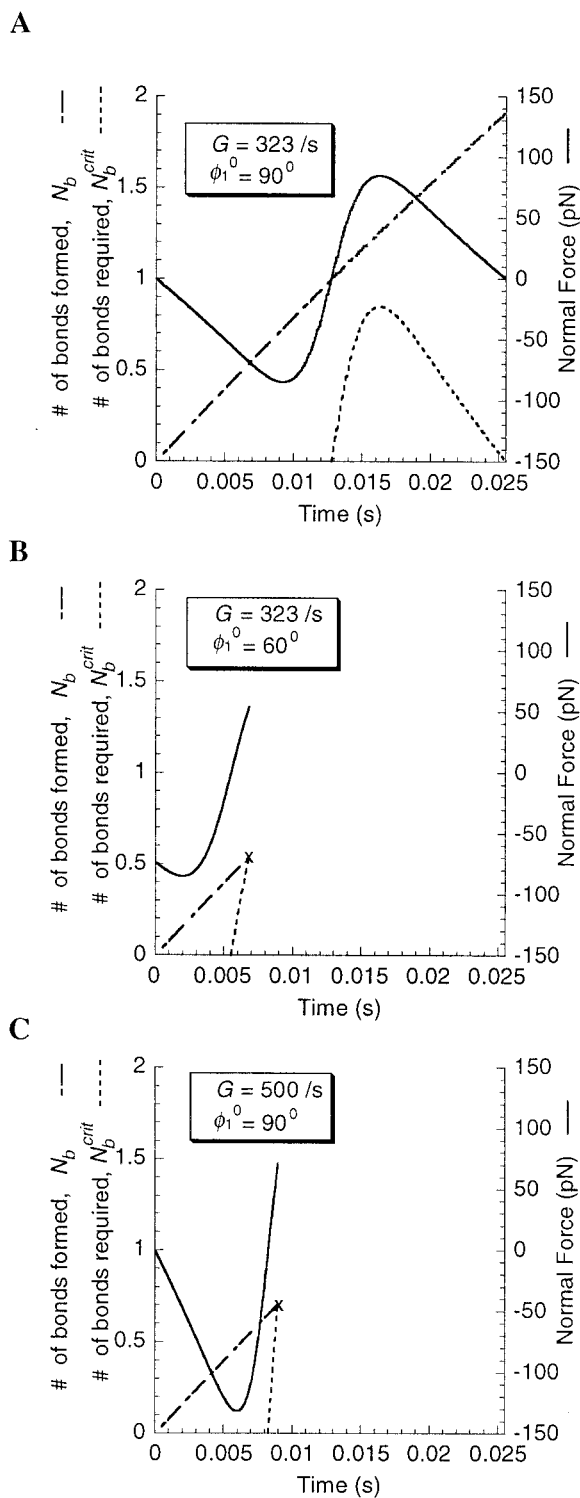
A

B

C

FIGURE 3 Interparticle force and bond formation following particle collision. A range of interparticle collisions with $\theta_1{}^0 = 90°$ were analyzed under primary flow conditions. The cases presented here are: (*A*) head-on collision ($\phi_1{}^0 = 90°$) at $G = 323$/s; (*B*) off-center collision ($\phi_1{}^0 = 60°$) at $G = 323$/s; and (*C*) head-on collision ($\phi_1{}^0 = 90°$) at $G = 500$/s. In each case, the temporal evolution of interparticle bonds, doublet orientation, and inter–particle force was estimated by solving the deterministic cell adhesion model (Eqs. 7 and 10–12). At each time point, the critical number of bonds required to hold the doublet together was calculated by dividing the

ing a tensile force. We examined how these hydrodynamic parameters may influence bond formation and the transition of an interacting doublet into a stable aggregate. An analysis of interparticle force and bond formation under primary flow conditions was performed (Fig. 3) by solving the particle interaction and bond formation model (Eqs. 7 and 10–12) for different initial collision orientations. Here, a constant on-rate ($k_f^0 N_L$) of 1.01×10^{-3}/s was used for all the simulations, and the other kinetic parameters were set according to Table 1. Only collisions occurring in the plane corresponding to $\theta_1^0 = 90°$ were considered.

A head-on collision ($\phi_1^0 = 90°$) at a shear rate $G = 323$/s was used as a reference to monitor the effects of varying forces and attachment times (Fig. 3 *A*). It should be noted that this is a hypothetical situation, and, in reality, a head-on collision between particles is not possible because their relative velocity is zero before collision. However, we have chosen this case as a reference because this is an extreme case where the doublet enjoys the maximum attachment time. In this case, during the compressive/attachment phase, which lasted up to $t \sim 13$ ms, the bonds were not subjected to tensile stresses and $N_b^{crit} = 0$. During this time, one interparticle bond was formed. The number of bonds required for stable aggregate formation (N_b^{crit}) was calculated at each time step, by dividing the normal tensile force $F_{(3)}'$ (Eq. 7) with the bond strength (f_c). At $t \sim 16$ ms, the doublet was subjected to maximum tensile loading of ~ 85 pN, and, at this time, N_b was ~ 1.22, whereas N_b^{crit} was ~ 0.8. For this collision, because N_b was greater than N_b^{crit} at all times in the tensile/detachment phase, the collision was said to result in stable aggregate formation.

For the case of an off-center collision occurring at $\phi_1° = 60°$ at the same shear rate, the attachment time was shorter (~ 5 ms), and only ~ 0.4 bonds were formed in this time (Fig. 3 *B*). In the tensile/detachment phase, the rate of bond formation was not high enough and the criterion in Eq. 13 was violated. Complete bond breakage occurred upon loading with a force of ~ 55 pN at 6.5 ms.

Next, we considered a head-on collision occurring at a higher shear rate, $G = 500$/s. Increasing the shear rate caused both an increase in the magnitude of the applied tensile force and a reduction in the attachment time (Fig. 3 *C*). The attachment time in this case was ~ 8 ms, and ~ 0.65 bonds were formed in this time. The number of bonds formed in the attachment phase was lower than that for the reference collision (Fig. 3 *A*). Additionally, the bonds were subjected to a greater tensile force in the detachment phase.

total normal force by the bond strength ($f_c = 100$ pN). The kinetic parameters used are listed in Table 1. A constant lumped on-rate ($k_f^0 N_L$) of 1.01×10^{-3}/s was used for all the simulations. The point where cell detachment occurred according to Eq. 13 is denoted by X in panels B and C. The number of bonds is depicted by broken lines, and the interparticle tensile force is represented by a solid line.

The maximum tensile force at this shear rate was $\sim$132 pN (not shown). As seen, the steep increase in applied forces and the proportionate rise in N_b^{crit} with time in the detachment phase, was not matched by an adequate rate of bond formation. The criterion for stable aggregation (Eq. 13) was violated at a force of $\sim$70 pN (at $t \sim 8$ ms), and the collision did not result in stable aggregate formation.

Taken together, these results suggest that stable aggregate formation after particle collision is a function of the attachment time and the applied hydrodynamic forces. Varying the collision orientation affects the attachment time alone, whereas varying the shear rate alters both the force and the attachment time. Because both the collision orientation and the shear rate are dependent on the local flow characteristics, these results illustrate the strong dependence of cell aggregation kinetics on hydrodynamic parameters.

Kinetic parameters for modeling homotypic neutrophil aggregation

Experimental data for homotypic neutrophil aggregation obtained using a 1° cone–plate viscometer (Fig. 5c in Taylor et al., 1996) was fitted using our theoretical model to predict the variation in lumped on-rate ($k_f^0 N_L$) with shear rate (G) based on arguments detailed in Methods. The sample volume used for these experiments was 500
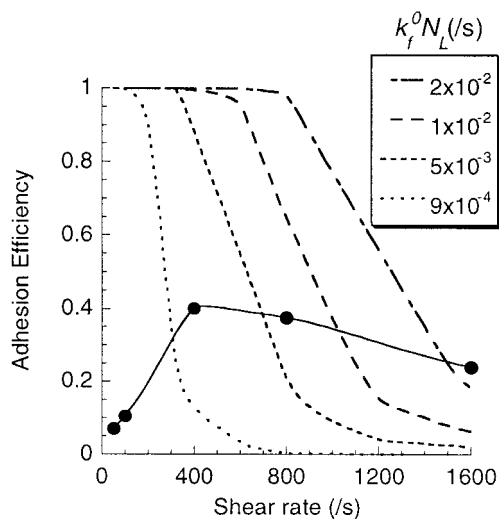

FIGURE 4 Modeling homotypic neutrophil aggregation data. Experimental data for neutrophil adhesion efficiency obtained using a 1° cone–plate viscometer (Taylor et al., 1996) is depicted by a solid line. These data were fitted using our mathematical model under primary flow conditions (Eqs. 7 and 10–13) by varying the kinetic lumped on-rate ($k_f^0 N_L$). During the simulations, the other kinetic parameters were kept constant (Table 1), while the on-rate $k_f^0 N_L$ was varied from 10^{-4}/s to 2×10^{-2}/s. For each of these on-rates, 1000 random collisions were simulated at each shear rate under primary flow conditions, and the adhesion efficiency (depicted by broken lines) was calculated as described in Methods. Points of intersection between theoretical curves and the experimental curve were used to determine the dependence of the on-rate on the applied shear rate G.
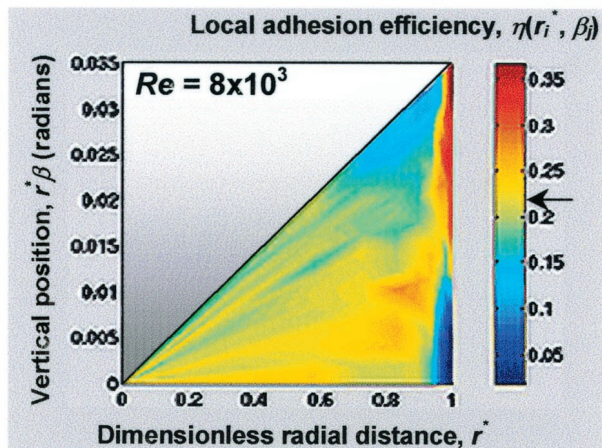
μl, and the maximum Re was $\sim$16,000 at 1600/s. Although not strictly valid, the flow was approximated using primary flow analysis to calculate approximate lumped on-rates at different shear rates. This provided us with a reasonably accurate description of the kinetics of neutrophil aggregation.

Briefly, the procedure for fitting the lumped on-rates ($k_f^0 N_L$) was as follows. Theoretical adhesion efficiencies were obtained as a function of shear rate using primary flow analysis. These adhesion efficiency curves were generated for a range of lumped on-rates while the other kinetic parameters were maintained constant (Table 1). On increasing shear rate (G) for a constant on-rate in these simulations, a decrease in adhesion efficiency was seen (Fig. 4). Points of intersection between theoretical curves and the experimental data yielded the appropriate on-rate value corresponding to each shear rate. Over the range of shear rates tested (100/s to 1600/s), our results indicated two distinct regimes for the dependence of the on-rate on the applied shear rate. 1) Below 400/s, the on-rate increased steeply with the shear rate from 10^{-4}/s at $G = 100$/s to 1.5×10^{-3}/s at $G = 400$/s. This region corresponds to the regime below the neutrophil threshold shear rate, where the adhesion efficiency increases with applied shear. 2) Beyond 800/s, the curve flattened out and the slope was much lower, with the on-rate increasing slowly from $\sim$7.0 $\times$ 10^{-3}/s at $G = 800$/s to $\sim$2.0 $\times$ 10^{-2}/s at $G = 1600$/s. This corresponds to shear rates greater than the threshold value where the adhesion efficiency decreases with increasing shear rate. The shear rate range from 400/s to 800/s was a transition region. The kinetic model with lumped on-rate parameters fitted as described above provides a phenomenological description of the effect of shear rate on homotypic neutrophil aggregation, and is applied to examine the role of secondary flow.

Secondary flow causes spatial variations in adhesion efficiency

Secondary flow causes spatial variations in the velocity gradient tensor. We examined whether cell adhesion efficiency may also vary with position in the viscometer under secondary flow conditions (Fig. 5). In this analysis, the $G_{(23)}$ element of the numerically computed local velocity gradient tensor $\mathbf{G}$ was used instead of the shear rate G at each grid point to estimate the lumped on-rate based on the curve fit in Fig. 4. All other kinetic parameters were from Table 1. We observed that secondary flow causes spatial variations in local adhesion efficiency in the viscometer. At $G = 1500$/s and Re $= 8 \times 10^3$ (sample volume $= 150 \mu$l for a 2° cone), the adhesion efficiency varied between 0 and $\sim$0.35 (Fig. 5 A) depending on spatial position in the device. A primary flow analysis at the same shear rate yielded a constant adhesion efficiency of 0.22 at all points in the viscometer. The variations in adhesion efficiency due to

A

Local adhesion efficiency, $\eta(r_i^*, \beta_j)$

Re = 8×10³

Vertical position, $r^*\beta$ (radians)

Dimensionless radial distance, r^*

B

Local adhesion efficiency, $\eta(r_i^*, \beta_j)$

Re = 3×10⁴

Vertical position, $r^*\beta$ (radians)
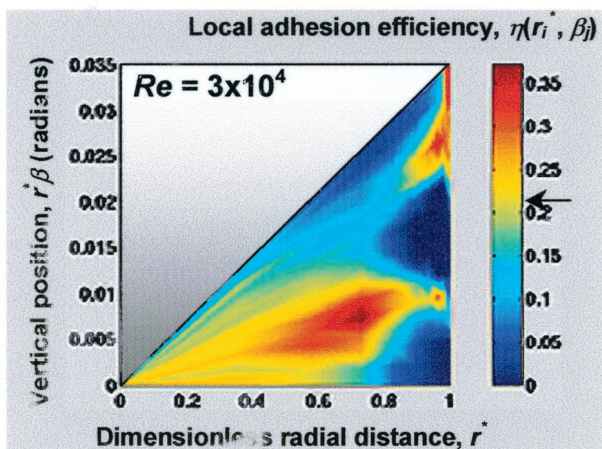
Dimensionless radial distance, r^*

FIGURE 5 Spatial variation of adhesion efficiency in the cone–plate viscometer. N_{col} (= 1000) weighted random collision orientations were generated for each grid point in the viscometer. The local adhesion efficiency, $\eta(r_i^*, \beta_j)$ at these grid points was calculated as described (Eq. 14). Modeling parameter values are listed in Table 1. The lumped on-rate was obtained by fitting experimental data with the deterministic model according to Fig. 4. Simulations were performed for a 2° viscometer at G = 1500/s. Spatial variation of adhesion efficiency is depicted for low and high Reynolds Numbers: (A) Re = 8 × 10³ and (B) Re = 3 × 10⁴. The two Re values correspond to sample volumes of ~150 and 1000 μl, respectively. Here, the curvilinear grid coordinates (r^*, β) were converted to cartesian coordinates according to: X coordinate = r^*; Y coordinate = $r^*\beta$. The arrow in the color-bar indicates the adhesion efficiency under primary flow conditions (~0.22).

secondary flow were most pronounced near the periphery of the device. At the periphery, regions near the plate surface had lower adhesion efficiencies than the primary flow value, whereas regions near the cone surface displayed higher efficiencies than that predicted by primary flow analysis. This is consistent with our previous results (H. Shankaran and S. Neelamegham, submitted for publication), which indicated higher forces and lower attachment times near the

plate surface, and lower forces and higher attachment times near the cone surface, compared to primary flow analysis. When the flow Reynolds number was increased to 3×10^4 at G = 1500/s (sample volume = 1000 μl for a 2° cone), deviations of adhesion efficiency from the primary flow value became more marked (Fig. 5 B). Although the adhesion efficiency still varied in the range from 0 to 0.35, there were many more, and larger regions of low and high efficiency values. Overall, our results indicate that spatial variations in velocity gradient induced due to nonlinear secondary flow may cause pronounced spatial variations in the adhesion efficiency.

Secondary flow causes a drop in overall adhesion efficiency

We examined how spatial variations in adhesion efficiency due to secondary flow may affect the overall collision-averaged efficiency for the entire viscometer (Fig. 6). These calculations were based on the generation of N_{col} = 1000 weighted random collision positions within the viscometer as detailed in Methods. The lumped on-rate for each collision was then calculated using the $G_{(23)}$ element of the numerically computed local velocity gradient tensor **G** and the data fit in Fig. 4. All other parameters were from Table 1. The overall adhesion efficiency was computed for a range of Re values and shear rates of 323/s and 1500/s, at two different cone angles. Increasing Re (= $R^2\Omega/v$) at a fixed shear rate corresponds to increasing the volume of the sample sheared. In Fig. 6, the sample volume corresponding to each Re is indicated on the top X axis for both the shear rates, so that investigators may use these charts to quantify the contribution of secondary flow in their experiments.

For a 1° cone (Fig. 6 A), at a shear rate of 323/s and a sample volume of 1000 μl (Re = 5120), secondary flow caused ~2% drop in the adhesion efficiency compared to primary flow. Although data for larger sample volumes of up to 80 ml is shown, this is not relevant from an experimental standpoint. Upon increasing the shear rate to 1500/s, we observed a 4% drop in adhesion efficiency at a sample volume of 1 ml (Re = 23,775), compared to primary flow conditions. For a 2° cone (Fig. 6 B), at a shear rate of 323/s, for a 1-ml sample (Re = 6460), secondary flow caused an 8% drop in the adhesion efficiency compared to primary flow. At the higher shear rate of 1500/s and a sample volume of 1 ml (Re = 30,000), the adhesion efficiency dropped by ~41% compared to primary flow.

These results indicate that increasing the Reynolds number beyond a certain limit causes a marked drop in the adhesion efficiency. This threshold Re value, beyond which secondary flow becomes prominent, is a strong function of the cone angle. At a shear rate of 323/s, secondary flow does not significantly alter the adhesion efficiency in the range of sample volumes and cone angles used in biological studies. However, at high shear rates of >1500/s, secondary flow
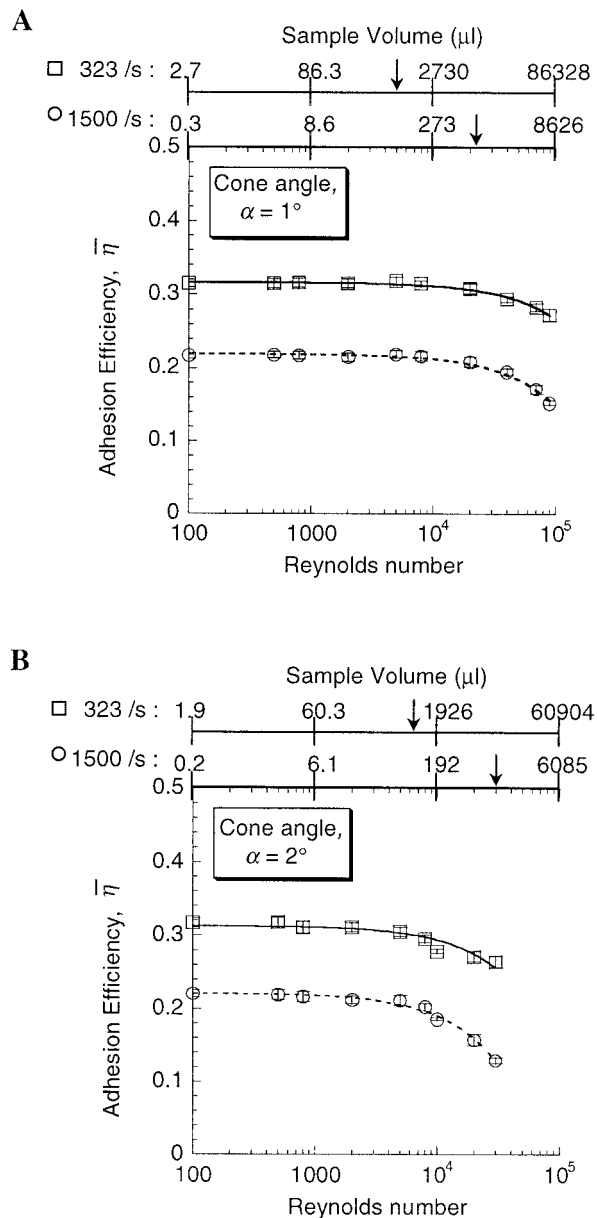
A

B

FIGURE 6 Effect of secondary flow on overall adhesion efficiency in the viscometer. The overall adhesion efficiency ($\bar{\eta}$) was calculated for a range of flow Reynolds numbers (Re) at two different shear rates viz. 323/s (□) and 1500/s (○). The dependence of adhesion efficiency on Re was examined for two viscometer cone angles: (A) 1° cone and (B) 2° cone. Different Re values at a constant shear rate were generated by varying the volume of the sample being sheared. The sample volume corresponding to each Re is therefore indicated on the top axis of the figure for the two different shear rates used. Arrows shown on top axis correspond to a sample volume of 1 ml. The adhesion efficiency is presented as mean ± SEM for 5 different random number seeds used for these calculations. Lines in the figure represent a smooth fit of the adhesion efficiency data.

causes a significant drop in adhesion efficiency compared to linear-primary flow for a 2° cone. Overall, these results suggest that cell adhesion rates in a cone–plate viscometer, in addition to being a function of the shear rate, depend on the cone angle and the sample volume.

Neutrophil binding kinetics in the aggregation phase

We attempted to validate our theoretical prediction that cell aggregation rates depend on the sample volume in a series of experiments where we monitored homotypic neutrophil aggregation rates following fMLP stimulus. Homotypic neutrophil aggregation following fMLP stimulus is a reversible process (Neelamegham et al., 1997). It is characterized by a rapid aggregation phase ($t < 60$ s), a stationary phase (60 s $\leq t \leq 120$ s), and a disaggregation phase ($t > 120$ s). During the aggregation phase, cells collide and rapidly form aggregates. In the stationary phase, these cells remain stable, and few new aggregates are formed. In the disaggregation phase, aggregate breakup occurs, and we see a marked increase in the singlet neutrophil population.

We examined how secondary flow may alter the aggregation of neutrophils (Fig. 7). Experiments were performed at shear rates of either 323/s or 1500/s, using a 2° cone–plate viscometer. Three different sample volumes (100 μl, 500 μl, 1000 μl) were used at each shear rate. These sample volumes correspond to Re values of 1390, 4070, and 6740, respectively, at 323/s. At 1500/s, these sample volumes correspond to Re values of 6460, 18,899, and 30,000, respectively. At 323/s, increasing sample volume did not cause a significant difference in neutrophil aggregation kinetics (Fig. 7 A). However, at 1500/s, increasing sample volume from 100 to 1000 μl caused an ~33% drop in the extent of aggregation at 10 s and an ~25% drop at 60 s (Fig. 7 B). We calculated the adhesion efficiency based on this data (Fig. 7 C). The adhesion efficiency dropped from 0.337 to 0.298 (~12% drop) when the sample volume was increased from 100 to 1000 μl at 323/s. However, the same change in sample volume caused an ~45% drop in adhesion efficiency (0.216 to 0.119) at 1500/s. Statistical analysis of the data established a significant decrease in the adhesion efficiency with increasing sample volume at 1500/s ($p = 0.0014$) but not at 323/s. The experimental results are consistent with our theoretical model, which predicted 8% and 41% drops in adhesion efficiency with reference to primary flow for a sample volume of 1000 μl at shear rates of 323/s and 1500/s, respectively. The dependence of the adhesion efficiency on sample volume can be explained based on the volume-dependent flow fields generated by nonlinear secondary flow in the cone–plate viscometer. These results thus partially validate our theoretical predictions.

Aggregate break-up in the disaggregation phase

We examined whether regions of high tensile force in the viscometer due to secondary flow may lead to volume-dependent disaggregation kinetics at $t > 120$ s (Fig. 8). Here, cells were first allowed to aggregate at a shear rate of 323/s for 120 s. Subsequently, the shear rate was either increased to 1500/s or maintained at 323/s. Samples were
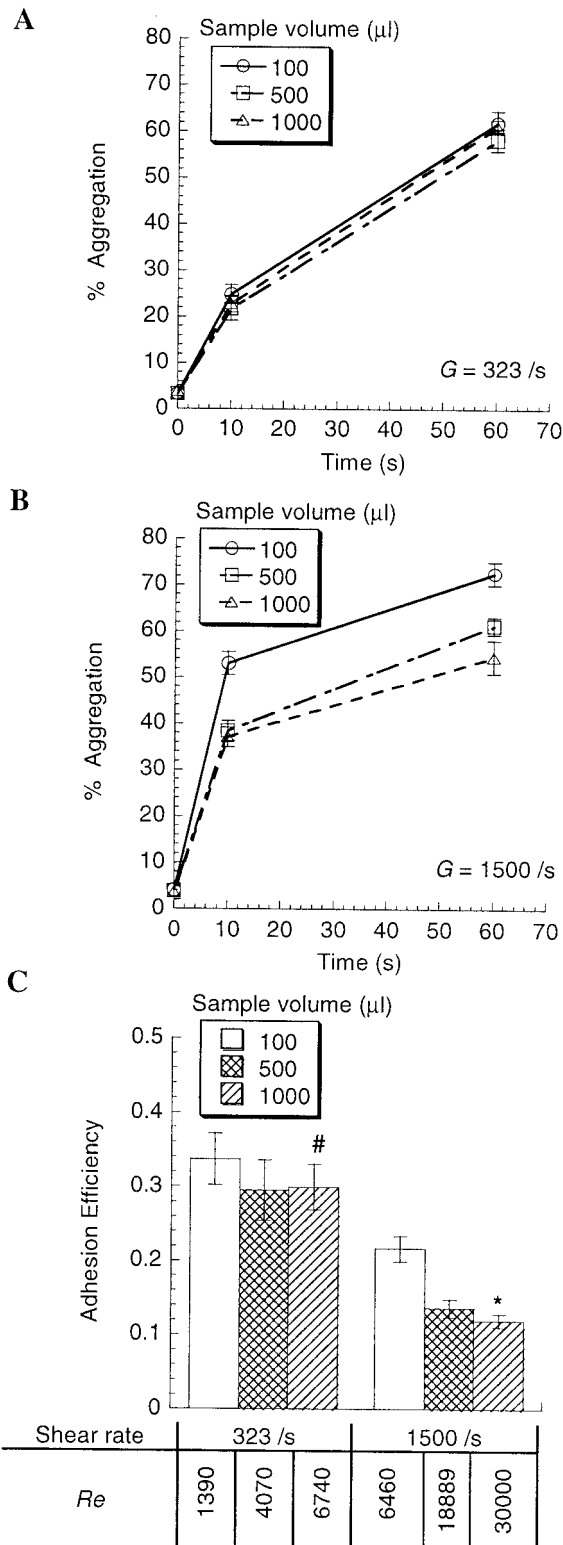
collected up to $t = 300$ s for flow-cytometric analysis and percent of aggregation was determined. Experiments were performed at two different sample volumes (150 and 1000 μl). For a shear rate of 1500/s in the disaggregation phase ($t > 120$ s), increasing the sample volume caused a consistent and reproducible augmentation in the disaggregation kinetics (Fig. 8 *A*). This was manifested as a more rapid drop in percent of aggregation for the larger-volume experiments. Simultaneously, the number of singlets in solution also increased at a faster rate for the 1000-μl experiments compared to the 150-μl experiments (data not shown). For a shear rate of 323/s in the disaggregation phase, increasing sample volume caused only a 6% increase in the extent of disaggregation at 300 s (Fig. 8 *B*). At 1500/s however, increasing sample volume caused a 22% increase in the extent of disaggregation at 300 s. Statistical analysis of the data established a significant augmentation in disaggregation rates with increasing sample volume at 1500/s ($p = 0.0001$) but not at 323/s. The results are consistent with our theoretical model of secondary flow, which predicted that collision-averaged hydrodynamic forces in the viscometer increase with sample volume (Fig. 2 *C*). This feature may augment the disaggregation kinetics with increasing sample volume. These results thus provide additional evidence to suggest the presence of a volume-dependent flow field in the viscometer, which may affect cell adhesion kinetics in suspension.

DISCUSSION

The cone–plate viscometer is used to study the role of shear forces in biological systems. Typical experiments are carried out under constant shear rate. They examine the role of hydrodynamic forces in altering the activation and adhesion function of cells in suspension, e.g., neutrophils and platelets, and those adherent on the plate surface, e.g., endothelial cells. In this paper, we examine how nonlinear secondary flow may alter cellular function by contributing to estimates of wall shear stress, interparticle collision frequency in suspension, and hydrodynamic forces during two-body interactions. We also describe a deterministic model for cellular adhesion in suspension, and apply it to examine selectin- and integrin-mediated neutrophil homotypic aggregation.

FIGURE 7　Neutrophil binding in the aggregation phase. Neutrophils at 1×10^6/ml were stimulated with 1 μM fMLP, and subjected to shear at either 323/s or 1500/s in a 2° cone–plate viscometer. Neutrophil aggregation kinetics was monitored in the aggregation phase (t = 0–60 s). The effect of secondary flow was studied by varying the volume of the sample being sheared (100, 500, or 1000 μl). Both the percent of aggregation (Eq. 16) and the adhesion efficiency were determined as described in Methods.

The variation of percent of aggregation with time is presented for: (*A*) $G = 323$/s and (*B*) $G = 1500$/s. (*C*) Dependence of adhesion efficiency on sample volume for low (323/s) and high shear rates (1500/s). The Re value corresponding to each shear rate and sample volume is given in table format below panel C. #, Efficiency at 1000 μl is not significantly different from that at 100 μl for $G = 323$/s ($p = 0.1$); *, $p = 0.0014$ for 1000 μl compared to 100 μl at 1500/s. Results are mean $\pm$ SEM for $N = 9$ independent experiments.
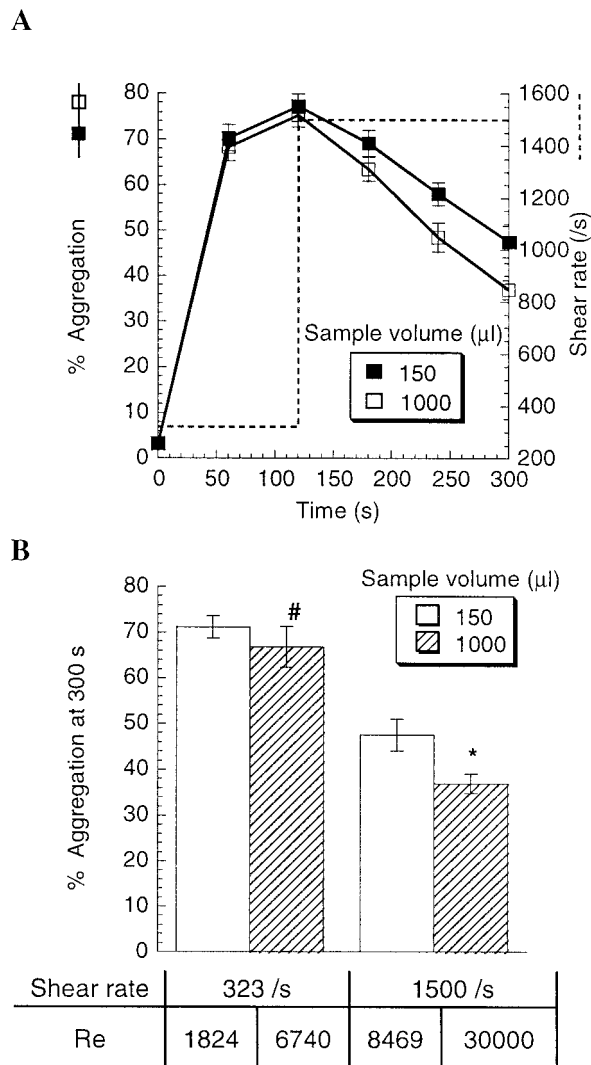
FIGURE 8 Neutrophil aggregates in the disaggregation phase. Neutrophils at a concentration of 1×10^6/ml were stimulated with 1 μM fMLP and sheared at 323/s in a 2° cone–plate viscometer for 120 s. The shear rate was then either step-increased to 1500/s or left unchanged. Samples were collected at regular intervals up to the 300 s and percent of aggregation (Eq. 16) was calculated. Experiments were performed with two different sample volumes (150 and 1000 μl). (A) Variation in percent of aggregation with sample volume for experiments where G was step-increased to 1500/s in the disaggregation phase ($t > 120$ s). Broken lines depict shear rate profile, and solid lines denote percent of aggregation data. (B) Extent of aggregation at the 300-s time point for 150- and 1000-μl samples subjected to either low (323/s) or high (1500/s) shear rates in the disaggregation phase ($t > 120$ s). Re corresponding to each shear rate and sample volume is given in table format below panel B. #, Percent of aggregation at 1000 μl is not significantly different from that at 150 μl for $G = 323$/s ($p = 0.21$); *, $p = 0.0001$ for 1000 μl compared to 150 μl at 1500/s. Results are mean ± SEM for $N = 6$–10 independent experiments.

Fluid Reynolds number and cone angle characterize flow in the viscometer

Dimensional analysis of the equations governing the flow in the viscometer reveal that the velocity field in the cone–plate viscometer is a function of two parameters: the flow Reynolds number Re ($= R^2\Omega/\nu$), and the cone angle α. Increasing either of these parameters results in an increase in secondary flow. We have recently shown (H. Shankaran and S. Neelamegham, submitted for publication) that, for a 2° cone, primary flow is not a reasonable approximation for flow at Re greater than 1000. This lower bound value of Re, above which secondary flow is prominent, is higher for viscometers with smaller cone angles.

Secondary flow causes spatial variations in the flow within the viscometer. As a result, at any given apparent shear rate (G), regions of both higher and lower local shear rate result. The local shear rates when volume-averaged approximately yield the apparent shear rate (data not shown). This causes a sort of "shear-averaging" of various features within the viscometer. Hence, although secondary flow is prominent at relatively low Re ($\sim$1000), depending on the nature of the biophysical measurements and due to shear-averaging, the effects of the nonlinear nature of secondary flow may only be apparent/measured at a much higher Re.

From a practical standpoint, besides shear rate, cone angle and sample volume are also important parameters influencing experimental results. In this regard, the dependence of secondary flow on Re implicitly makes it dependent on the radius (R) of the sample being sheared, which in turn is a function of sample volume. Hence, changing the sample volumes in experiments at the same angular velocity may alter the nature of particle interactions and the wall shear stress.

Secondary flow induces spatial variations in the collision frequency, interparticle force, and attachment time within the viscometer

Results of our particle interaction analysis indicate that collision frequency, interparticle force, and attachment time vary with position in the viscometer (H. Shankaran and S. Neelamegham, submitted for publication). This is a direct consequence of the positional variations in the velocity gradient tensor induced by the nonlinear nature of flow. Depending on the spatial coordinates, both the collision frequency and interparticle force varied from 0.3 to 4.8 times their corresponding primary flow values at Re $= 3 \times 10^4$ and $\alpha = 2°$ (H. Shankaran and S. Neelamegham, submitted for publication). The deviation from primary flow was more pronounced at the edge of the device. Due to the shear-averaging of these features in the viscometer, however, the overall collision frequency and inter-particle forces are only slightly different from that predicted by primary flow analysis. Although the volume-averaged collision frequency under secondary flow in the range examined was within 3% of that predicted by primary flow analysis, the

collision-averaged maximum normal force was up to ~35% higher.

Time-varying shear stresses due to secondary flow may contribute to shear-induced platelet aggregation

Platelet aggregation is a consequence of the bridging of platelet surface glycoprotein complexes including GpIb/IX/V and GpIIb-IIIa, by serum factors like fibrinogen and von Willebrand factor (vWF) (Hellums et al., 1987; Ikeda et al., 1991; Kroll et al., 1996). Although the receptor complexes in resting or unactivated platelets do not bind the bridging ligand, high shear forces are thought to induce conformational changes in the GpIb/IX/V complex or vWF, and consequent platelet aggregation via the bridging molecule vWF (Kroll et al., 1996; Peterson et al., 1987). This agonist-independent phenomenon is referred to as shear-induced platelet aggregation (SIPA). Based on studies carried out in the cone–plate viscometer and other such shearing devices, it is currently felt that this shear-mediated pathway may regulate platelet activation and aggregation function under flow conditions such as those observed in stenosed arteries (Hellums et al., 1987; Ikeda et al., 1991; Jen and McIntire, 1984).

SIPA is normally studied in the cone–plate viscometer at shear rates of ~10,000/s. The sample volumes used in these experiments are typically ~500 μl and they correspond to Re values from 5×10^4 to 1.3×10^5 depending on the cone angle. These conditions coincide with extremely prominent secondary flow conditions in the viscometer, and marked positional variations in the velocity gradient within the device. Platelets subjected to fluid flow under these conditions, would circulate with the fluid streamlines, and would be exposed to a range of shear conditions. Hence it seems possible that time-varying shear stresses, in addition to constant high shear, may contribute significantly to SIPA data obtained from the cone–plate viscometer. This proposition is in agreement with limited parallel-plate flow chamber experimental data (Holme et al., 1997), which suggest that sudden changes in the shear stress rather than shear itself triggers platelet activation and micro-particle formation.

Possible role of secondary flow in endothelial cell mechanotransduction

The mechanotransduction of endothelial cells has been studied both in the parallel plate flow chamber (Kuchan and Frangos, 1994) and the cone–plate viscometer (Dewey, 1984; Tsao et al., 1996). As was the case for SIPA, both variations in shear stress and the magnitude of applied shear appear to be important parameters regulating mechanotransduction. In the parallel plate flow chamber, cells subjected

to steady shear increase the amount of nitric oxide released approximately linearly with applied wall shear stress in the range of 1–10 dynes/cm^2 (Frangos et al., 1985). Experiments have also been conducted in cone–plate viscometers at apparent wall shear stresses of ~20 dynes/cm^2 (estimated using primary flow analysis) (Dewey, 1984; Tsao et al., 1996). These shear rates are high enough for the onset of secondary flow in the medium. From our analysis, it can be seen that secondary flow may cause an ~5-fold increase in wall shear stress at the edge of the viscometer under similar conditions. Thus, in these experiments, some cells may experience shear stresses of up to ~100 dynes/cm^2. Ignoring secondary flow effects in these experiments could lead to incorrect conclusions regarding the range of shear stresses required for endothelial cell mechanotransduction.

Effect of secondary flow on neutrophil/cellular adhesion efficiency

To examine the role of secondary flow on cellular aggregation, we examined the case of L-selectin and β_2-integrin-mediated homotypic neutrophil aggregation. These experiments and associated calculations accounted for the detailed secondary flow within the viscometer. The model assumes that integrins at low shear and selectins at high shear rates limit the rate of neutrophil aggregation. Here, we observed that the lumped on-rate parameter $k_f^0 N_L$ was in the range of 10^{-4} to 10^{-2}/s for neutrophil–neutrophil adhesion. Although some of the assumptions of this work differ from those of Tandon and Diamond (1998), it is interesting to note that their estimate of on-rate lies within the range reported here.

Our model suggests that secondary flow may cause positional variations in adhesion efficiency in the device and a drop in the overall collision-averaged efficiency for the entire viscometer. This is in contrast to primary flow conditions, where the adhesion efficiency is the same throughout the viscometer and is a function of the shear rate alone. The effect of secondary flow on adhesion efficiency can be explained with reference to our calculations of particle hydrodynamics in the viscometer. Secondary flow causes positional variations in the fluid velocity gradient, interparticle forces, and attachment times. These features contribute to the observed spatial variations in the adhesion efficiency. The effect of secondary flow on cell adhesion efficiency is a strong function of the cone angle. Reducing the cone angle significantly increases the threshold Re value beyond which secondary flow influences cell aggregation kinetics.

Under secondary flow conditions, the dependence of adhesion efficiency on Re makes it a function of the sample volume. This feature can be used to distinguish between the contributions of nonlinear secondary flow and linear-primary flow on cell aggregation kinetics in the viscometer. With this objective, we performed neutrophil aggregation experiments with varying sample volumes at different shear

rates in a 2° cone–plate viscometer. At a shear rate of 1500/s, the adhesion efficiency dropped significantly (~45%) when the sample volume was varied from 100 to 1000 μl. These experimental results closely match theoretical predictions of adhesion efficiency under secondary flow conditions. In addition, experimental results also indicated that secondary flow causes an augmentation in the disaggregation rates of pre-formed neutrophil aggregates. These results can be explained in light of the fact that increasing sample volume at a fixed shear rate causes an increase in the flow Reynolds number and secondary flow effects. Thus, the volume dependence of the extent of cell aggregation seen experimentally provides partial validation for our theoretical model.

Overall, we have demonstrated that nonlinear flow features may exist in the range of shear rates used in conventional biological studies, and that these features may significantly alter the response of cells to hydrodynamic shear. Although the presence of nonlinear or transient flow is inevitable in most experimental devices used in biological experiments, especially at high shear rates, the analysis framework described here provides a systematic methodology both to design experiments and to interpret in vitro data obtained from the viscometer under these conditions. It also provides a general scheme to model particle interactions in nonlinear flow, which can be applied to other shearing devices where the flow may be complex and nonlinear. Further, our theoretical model combined with cone–plate viscometer experiments may be a useful tool to study the effects of spatial and temporal force variations, induced by nonlinear flow, on the biological function of cells.

REFERENCES

Aidun, C. K., Y. Lu, and E. J. Ding. 1998. Direct analysis of particulate suspensions with inertia using the discrete Boltzmann equation. *J. Fluid Mech.* 373:287–311.

Akima, H. 1970. A new method of interpolation and smooth curve fitting based on local procedures. *J. ACM.* 17:589–602.

Aris, R. 1989. Vectors, Tensors and the Basic Equations of Fluid Mechanics. Dover Publications Inc., New York.

Arp, P. A., and S. G. Mason. 1977. The kinetics of flowing dispersions. VIII. Doublets of rigid spheres (Theoretical). *J. Colloid Interf. Sci.* 61:21–43.

Bell, G. I. 1978. Models for the specific adhesion of cells to cells. *Science.* 200:618–627.

Brenner, H., and M. E. O'Neill. 1972. On the Stokes resistance of multiparticle systems in a linear shear field. *Chem. Eng. Sci.* 27:1421–1439.

Chang, K., and D. A. Hammer. 1999. The forward rate of binding of surface-tethered reactants: effect of relative motion between two surfaces. *Biophys. J.* 76:1280–1292.

Chen, S., and T. A. Springer. 1999. An automatic braking system that stabilizes leukocyte rolling by an increase in selectin bond number with shear. *J. Cell Biol.* 144:185–200.

Dewey, C. F. 1984. Effects of fluid flow on living vascular cells. *J. Biomech. Eng.* 106:31–35.

Evans, C. W., and J. Proctor. 1978. A collision analysis of lymphoid cell aggregation. *J. Cell Sci.* 33:17–36.

Evans, E., and K. Ritchie. 1997. Dynamic strength of molecular adhesion bonds. *Biophys. J.* 72:1541–1555.

Fewell, M. E., and J. D. Hellums. 1977. The secondary flow of Newtonian fluids in cone-and-plate viscometers. *Trans. Soc. Rheol.* 21:535–565.

Finger, E. B., K. D. Puri, R. Alon, M. B. Lawrence, U. H. von Andrian, and T. A. Springer. 1996. Adhesion through L-selectin requires a threshold hydrodynamic shear. *Nature.* 379:266–269.

Frangos, J. A., S. G. Eskin, L. V. McIntire, and C. L. Ives. 1985. Flow effects on prostacyclin production by cultured human endothelial cells. *Science.* 227:1477–1479.

Goto, S., Y. Ikeda, E. Saldivar, and Z. M. Ruggeri. 1998. Distinct mechanisms of platelet aggregation as a consequence of different shearing flow conditions. *J. Clin. Invest.* 101:479–486.

Guerra, V. O., R. A. Tapia, and J. R. Thompson. 1976. A random number generator for continuous random variables based on an interpolation procedure of Akima. *In* The Ninth Interface Symposium on Computer Science, and Statistics, D. C. Hoaglin and R. E. Welsch, editors. Prindle, Weber, and Schmidt, Boston. 228–230.

Guyer, D. A., K. L. Moore, E. B. Lynam, C. M. G. Schammel, S. Rogelj, R. P. McEver, and L. A. Sklar. 1996. P-selectin glycoprotein ligand-1 (PSGL-1) is a ligand for L-selectin in neutrophil aggregation. *Blood.* 88:2415–2421.

Haidekker, M. A., N. L'Heureux, and J. A. Frangos. 2000. Fluid shear stress increases membrane fluidity in endothelial cells: a study with DCVJ fluorescence. *Am. J. Physiol. Heart Circ. Physiol.* 278: H1401–H1406.

Hammer, D. A., and D. A. Lauffenburger. 1987. A dynamic model for receptor-mediated cell adhesion to surfaces. *Biophys. J.* 52:475–487.

Hellums, J. D., D. M. Peterson, N. A. Stathopoulos, J. L. Moake, and T. D. Giorgio. 1987. Studies on the mechanisms of shear-induced platelet activation. *In* Cerebral Ischemia and Hemorheology. A Hartman and W. Kushinsky, editors. Springer-Verlag. Berlin. 81–89.

Hentzen, E. R., S. Neelamegham, G. S. Kansas, J. A. Benanti, L. V. McIntire, C. W. Smith, and S. I. Simon. 2000. Sequential binding of CD11a/CD18 and CD11b/CD18 defines neutrophil capture and stable adhesion to intercellular adhesion molecule-1. *Blood.* 95:911–920.

Holme, P. A., U. Orvim, M. J. A. G. Hamers, N. O. Solum, F. R. Brosstad, R. M. Barstad, and K. S. Sakariassen. 1997. Shear-induced platelet activation and platelet microparticle formation at blood flow conditions as in arteries with a severe stenosis. *Arterioscler. Thromb.* 17:646–653.

Ikeda, Y., M. Handa, K. Kawano, K. Tetsuji, M. Murata, Y. Araki, H. Anbo, Y. Kawai, K. Watanabe, I. Itagaki, K. Sakai, and Z. M. Ruggeri. 1991. The role of von Willebrand factor and fibrinogen in platelet aggregation under varying shear stress. *J. Clin. Invest.* 87:1234–1240.

Jen, C. J., and L. V. McIntire. 1984. Characteristics of shear-induced aggregation in whole blood. *J. Lab. Clin. Med.* 103:115–124.

Kishimoto, T. K., M. A. Jutila, E. L. Berg, and E. C. Butcher. 1989. Neutrophil Mac-1 and MEL-14 adhesion proteins inversely regulated by chemotactic factors. *Science.* 245:1238–1241.

Kroll, M. H., J. D. Hellums, L. V. McIntire, A. L. Schafer, and J. L. Moake. 1996. Platelets and shear stress. *Blood.* 88:1525–1541.

Kuchan, M. J., and J. A. Frangos. 1994. Role of calcium and calmodulin in flow-induced nitric oxide production in endothelial cells. *Am. J. Physiol. Cell Physiol.* 266:C628–C636.

Lawrence, M. B., S. G. Kansas, E. J. Kunkel, and K. Ley. 1997. Threshold levels of fluid shear promote leukocyte adhesion through selectins (CD62L, P, E). *J. Cell. Biol.* 136:717–727.

Merkel, R., P. Nassoy, A. Leung, K. Ritchie, and E. Evans. 1999. Energy landscapes of receptor–ligand bonds explored with dynamic force spectroscopy. *Nature.* 397:50–53.

Moake, J. L., N. A. Turner, N. A. Stathopoulos, L. Nolasco, and J. D. Hellums. 1988. Shear-induced platelet aggregation can be mediated by vWF released from platelets, as well as by exogenous large or unusually

large vWF multimers, requires adenosine diphosphate, and is resistant to aspirin. *Blood.* 71:1366–1374.

Neelamegham, S., A. D. Taylor, A. B. Burns, C. W. Smith, and S. I. Simon. 1998. Hydrodynamics shear reveals distinct roles for LFA-1 and Mac-1 in neutrophil adhesion to ICAM-1. *Blood.* 92:1626–1638.

Neelamegham, S., A. D. Taylor, J. D. Hellums, M. Dembo, C. W. Smith, and S. I. Simon. 1997. Modeling the reversible kinetics of neutrophil aggregation under hydrodynamic shear. *Biophys. J.* 72:1527–1540.

Neelamegham, S., A. D. Taylor, H. Shankaran, C. W. Smith, and S. I. Simon. 2000. Shear and time dependent changes in Mac-1, LFA-1, and ICAM-3 binding regulate neutrophil homotypic adhesion. *J. Immunol.* 164:3798–3805.

Ohno, M., G. H. Gibbons, V. J. Dzau, and J. P. Cooke. 1993. Molecular and cellular biology: shear stress elevates endothelial cGMP: role of a potassium channel and G protein coupling. *Circulation.* 88:193–197.

Peterson, D. M., N. A. Stathopoulos, T. D. Giorgio, J. D. Hellums, and J. L. Moake. 1987. Shear-induced platelet aggregation requires von Willebrand Factor and platelet membrane glycoproteins Ib and IIb-IIIa. *Blood.* 69:625–628.

Puri, K. D., S. Chen, and T. A. Springer. 1998. Modifying the mechanical property and shear threshold of L-selectin adhesion independently of equilibrium properties. *Nature.* 392:930–933.

Savins, J. G., and A. B. Metzner. 1970. Radial (secondary flows) in rheogoniometric devices. *Rheologica Acta.* 9:365–373.

Schmidtke, D. W., and S. L. Diamond. 2000. Direct observation of membrane tethers formed during neutrophil attachment to platelets or P-selectin under physiological flow. *J. Cell Biol.* 149:719–729.

Sdougos, H. P., S. R. Bussolari, and C. F. Dewey. 1984. Secondary flow and turbulence in a cone-and-plate device. *J. Fluid Mech.* 138:379–404.

Shao, J., H. P. Ting-Beall, and R. M. Hochmuth. 1998. Static and dynamic lengths of neutrophil microvilli. *Proc. Natl. Acad. Sci. U.S.A.* 95:6797–6802.

Simon, S. I., J. D. Chambers, E. Butcher, and L. A. Sklar. 1992. Neutrophil aggregation is β_2-integrin- and L-selectin-dependent in blood and isolated cells. *J. Immunol.* 149:2765–2771.

Smoluchowski, M. V. 1917. Versuch einer mathematischen theorie der koagulationskinetik kolloider losungen. *Z. Phys. Chem.* 92:129–168.

Springer, T. A. 1995. Traffic signals on endothelium for lymphocyte recirculation and leukocyte emigration. *Annu. Rev. Physiol.* 57:827–872.

Tandon, P., and S. L. Diamond. 1998. Kinetics of β_2-Integrin and L-Selectin bonding during neutrophil aggregation in shear flow. *Biophys. J.* 75:3163–3178.

Taylor, A. D., S. Neelamegham, J. D. Hellums, C. W. Smith, and S. I. Simon. 1996. Molecular dynamics of the transition from L-selectin- to β_2-integrin-dependent neutrophil adhesion under defined hydrodynamic shear. *Biophys. J.* 71:3488–3500.

Tha, S. P., and H. L. Goldsmith. 1986. Interaction forces between red cells agglutinated by antibody. I. Theoretical. *Biophys. J.* 50:1109–1116.

Tha, S. P., J. Shuster, and H. L. Goldsmith. 1986. Interaction forces between red cells agglutinated by antibody. II. Measurement of hydrodynamic force of breakup. *Biophys. J.* 50:1117–1126.

Tsao, P. S., R. Buitrago, J. R. Chan, and J. P. Cooke. 1996. Fluid flow inhibits endothelial adhesiveness nitric oxide and transcriptional regulation of VCAM-1. *Circulation.* 94:1682–1689.

Wagner, C. T., W. Durante, N. Christodoulides, J. D. Hellums, and A. I. Schafer. 1997. Hemodynamic forces induce the expression of heme oxygenase in cultured vascular smooth muscle cells. *J. Clin. Invest.* 100:589–596.